IMPROVING THE ACCURACY OF FLUX CALCULATIONS IN RAY TRACING SIMULATIONS FOR SOFT X-RAY BEAMLINES

Chemical Physics 5P Thesis

Patrick Wang
April 2024

Submitted in partial fulfilment of the requirements
for the degree of Master of Chemical Physics (Hons)
to the
School of Chemistry
College of Science and Engineering
University of Edinburgh

Total combined wordcount: 6982 (9914 incl. Methodology)
Supervisors: Dr Andrew Walters, Murilo Bazan da Silva, and Dr Joshua S. Gibson

Declaration

The contents of this report have been approved by the supervisor running this project and I declare the work as a non-confidential project.

I declare that this thesis was composed by myself, that the work contained herein is my own except where explicitly stated otherwise in the text, and that this work has not been submitted for any other degree or qualification.

Patrick Wang

Oxford, April 2024

Acknowledgements

I would like to acknowledge and give my warmest thanks to my supervisors: Andrew and Murilo. The unwavering support that they provided during the course of the project was crucial to the success. *Specifically*:

I am grateful for Andrew's time and patience in debugging the code, answering questions about *SHADOW*, computing the grating efficiencies, and too many things to list here.

I am grateful to Murilo for being supportive in every way he can and offering the computing resources.

I thank Dr Joshua S. Gibson for his patience and time in reading over the draft and providing helpful feedback.

I thank Prof Georg Held for his prompt reply to requests for data and questions in general.

I am sincerely grateful to my friends Leo, Tihana, and Zhishuo for their companionship and emotional support.

I express my gratitude to everyone at the Diamond Light Source for being welcoming and making me feel right at home.

Acronyms

EXAFS extended X-ray absorption fine structure

FoM figure of merit

ID insertion device

OE optical element

PDF probability distribution function

PGM plane grating monochromator

XANES X-ray absorption near-edge structure

XAS X-ray absorption spectroscopy

XES X-ray emission spectroscopy

XPS X-ray photoelectron spectroscopy

Abstract

The advent of synchrotron radiation with high brilliance and coherence has brought forth a variety of novel characterisation techniques to understand reactions under challenging conditions. In the soft X-ray range, techniques such as X-ray absorption spectroscopy have played an important role in the fields of surface, material, and battery research. Techniques such as X-ray photoelectron spectroscopy (XPS) can provide highly surface-sensitive structural information. This opens the possibility for detailed studies of *e.g.* heterogeneous copper catalyst poisoning in methanol synthesis by Swallow *et al.* [1] A universal component to all soft X-ray beamlines is the plane grating monochromator (PGM), which at present is poorly simulated in the context of ray-tracing. Due to its complex and non-intuitive geometry, even state-of-the-art ray-tracing software like *SHADOW*[2] cannot correctly account for self blockages resulting in over-reporting flux in simulation. The requirement for manual input and verification makes a systematic and holistic simulation of a soft X-ray beamline extremely difficult. This thesis presents the formal analytical expressions for geometrical quantities within a PGM. The expressions are packaged in callable functions in `python` to interact with *SHADOW*'s application programming interface (API). This enables the automatic handling of ray-tracing calculations natively within *SHADOW*. In addition, a set of tools are proposed which are compiled to enable a more robust workflow for simulating any general soft X-ray beamline with a PGM. The methodology was verified extensively by performing systematic calculations for beamline B07c at the Diamond Light Source. Calculations confirmed the existence of higher order contamination and its scope. A figure of merit function is also proposed that can quickly inform an optimal mode of operation for the B07c beamline and other beamlines in general.

Contents

List of Figures

List of Tables

1 Introduction

More complex equipment is continuously being developed to study better approximations to ‘real-world’ systems and their underlying chemistry. As experiments become more challenging, researchers often see diminishing returns in experimental data. The demands for optimising the usage of these novel facilities directly drive the development of complex physical models. Universal to practically all soft X-ray beamlines is the plane grating monochromator (PGM). Both the design of the PGM and the beamline as a whole are ideally optimised with detailed calculations. Presently, this is done through a technique called *ray-tracing*, where the trajectories of photons propagating through an optical system are *traced*. Coupled with the advent of powerful computers, the relevance of X-ray ray-tracing simulations in designing better experimental equipment is ever-growing, the importance of which will only increase in light of new developments in free electron lasers and 4th generation synchrotrons.

Currently, no robust method exists for simulating the plane grating monochromator (PGM), a key component of beamlines, that require monochromatic light of energies up to ca. 2500 eV. The most effective technique available for deriving the theoretical performance of a beamline is ray-tracing, which, in essence, is the calculation of the trajectories of photons as they are propagated through an optical system. The same technique is more frequently applied to visible light in the field of computer graphics and 3D animation. Simulation is technically possible presently with ray-tracing software like *SHADOW* [2] but such calculations fail to account for the loss of flux due to certain geometrical blockages whilst the PGM is in operation. Practically, this corresponds to the beam footprint falling off the optics and clipping the optics nearing the limits of the energy range of the PGM. Such shortfalls make systematic and iterative calculations – *i.e.*, of transmitted flux as a function of energy – extremely difficult. The lack of access to reliable simulation results means that beamline designers may fail to spot certain problems; this issue has already led to challenges in operation for beamline B07c at the Diamond Light Source (Diamond), UK’s national synchrotron facility. Anecdotal evidence from beamline staff and users suggests a significant problem of higher harmonic characterisation, where undesired photon energies are not adequately filtered. This can have direct consequences where signals from absorptions by different species cannot be distinguished. Through the use of the technique developed as part of the work for this thesis, the issue can be confirmed with theoretical calculation. Furthermore, the results can inform an optimised mode of operation. The newly developed methodology, which can be applied to simulate any general soft X-ray beamline that has a PGM, is presented.

In this section, the basic principles of synchrotron radiation are introduced, along with its applicability in the chemical sciences. An introduction to the PGM and the ray-tracing technique is discussed to highlight the challenges of simulating PGMs. This introduction sets the stage for understanding specifically the challenge of higher harmonic contamination in soft X-ray beamlines and the detrimental effect it can have on the quality of the data. This discussion serves to provide the motivation for developing more robust ray-tracing methodologies that would help resolve potential issues in future beamlines from the outset.

1.1 Synchrotron Radiation

Synchrotrons belong to a special class of particle accelerators. In essence, magnetic fields are applied to electrons travelling at relativistic speeds to force a circular trajectory, and the energy lost due to the change in acceleration is given off as electromagnetic radiation in the direction of travel; it is a special form of *bremsstrahlung* radiation, which can be used to perform a wide range of techniques probing a material's chemical and structural properties. Electrons are first produced by thermionic emission and then go through the linear accelerator (Linac). The booster ring further accelerates the electrons to the desired energy, 3 GeV for Diamond, followed by injection into the storage ring. In the storage ring, along the path of the electrons are a series of bending magnets and insertion devices that cause the electrons to change their trajectory and, hence, their acceleration. Such perturbation will cause the lost kinetic energy to be emitted as photons. The light is then directed via a series of optics into beamlines, where experiments take place [3].

This discovery led to the conception of the first-generation synchrotron facilities in the 1970s [4]. Historically, the radiation was used parasitically, as the machines were not designed for synchrotron radiation studies. Subsequently, newer synchrotrons were built with the idea that such facilities would be dedicated to light generation. Diamond, where this research was conducted, is an example of a 3rd generation synchrotron that uses undulators and bending magnets as sources of radiation. Despite differences in the properties of light produced by differing synchrotrons, the archetypal synchrotron light will have the following main properties:

- high intensity,
- pulsed with duration on the order of picoseconds,

- high beam stability,
- broad spectral range from infrared to hard X-rays.

Compared to traditional lab X-ray sources, synchrotrons have superior flux and spectral range. It is these advantages that have led to a huge surge in demand for beam time at synchrotron facilities worldwide. Specifically in the soft X-ray region (photon energies up to ca. 3000 eV), the advent of synchrotrons has enabled new techniques that have become ubiquitous in chemistry and material science. There are four overarching themes:

1. Spectroscopy
2. Diffraction
3. Microscopy
4. Scattering

All these techniques take advantage of the benefits that synchrotron radiation offers and may be of interest to the modern chemist; spectroscopic techniques are highlighted in specific detail as to provide relevant background for the subsequent discussion of ray-tracing simulations carried out for a spectroscopy beamline (B07c) at Diamond [5]. Outside the realm of spectroscopy, techniques such as: resonant magnetic diffraction is useful for selective measurements of atomic spin and orbital correlations [6], resonant elastic soft X-ray scattering is used to study spatial modulations of orbitals in solid materials [7]. The small scattering angles and the wavelength make soft X-ray techniques possess a unique bond orientation sensitivity [8], particularly useful in the probing of nanoscale structures of polymeric systems. Reviews are abundant for soft X-ray techniques not otherwise discussed in this work [6–10].

In the soft X-ray region, spectroscopies can be separated into absorption and emission spectroscopies. X-ray absorption spectroscopy (XAS) probes primarily the excitation from the ground state to the excited state, directly examining the local density of unoccupied states. This can give extensive information on structure of molecular orbitals and hence possible bonding environments. X-ray emission spectroscopy (XES) probes the decay from the excited state. Complementary structural information can usually be obtained by using a combination of techniques. The X-ray absorption spectrum of any material is characterised by a sharp rise in X-ray absorption at specific binding energies. These sharp changes are referred to as absorption edges, which correspond to the minimum energy required to excite a core electron. The absorption by an electron in the $1s$ orbital is referred to as K-edge absorption and L-edge for $2s$ and $2p$ electrons respectively. Spectroscopy over the energy range where the edges reside is referred to as X-ray absorption near-edge structure (XANES), which directly probes the density of states at the excited level and, consequently, is capable of providing extensive information on the oxidation state and coordination of metal atoms of interest [11]. By performing XAS over a range of energies, one can examine both the transition from core electronic states to excited states (LUMO) as well as the continuum where the X-ray delivers sufficient energy for the ejection of a photoelectron. Over the energy range where a photoelectron is emitted, the technique is extended X-ray absorption fine structure (EXAFS) if the absorption of light is measured. Should an energy of the ejected photoelectron be measured, the technique is termed X-ray photoelectron spectroscopy (XPS). Such a photoelectron would allow elemental identification of the atom that ejected the electron using the known binding energy. An area which is frequently explored using these techniques is the elucidation of the structure of surfaces. Heterogeneous catalysis and electron correlations are just two of many areas of research made possible by XANES, EXAFS, and XPS [5, 12]. Often-times, structural information of surfaces are difficult to derive due to the long probing depth of photon-based techniques; this is addressed by probing the photoelectrons in XPS which offers significantly more surface sensitivity.

B07c is a part of the versatile soft X-ray (VerSoX) beamline at Diamond. Common to almost all work carried out at B07c is the focus on the chemical and compositional properties of surfaces, which are characterised using XANES and XPS.

1.2 Monochromation of Soft X-rays

The primary benefit of XAS is its sensitivity to local structure, a consequence of exciting the core electrons. This is only possible when the probing radiation is spectrally pure. Local information about core electrons would be lost if undesired signals arise from a spectrally impure beam. Specifically in the soft X-ray range, the main method to achieve monochromatic light is by using the dispersive property of a diffraction grating, a crystal which is etched on its surface mechanically or otherwise, with certain physical characteristics (lines per mm) and characterised by a grating period. Diffraction by a grating optic is governed by the grating equation:

$$n\lambda = g(\sin\alpha + \sin\beta) \tag{1}$$

where n takes integer values and is the diffraction order, g is the grating period, α and β are angles of incidence and diffraction respectively. The parameters are presented in Fig. 1. Conventionally, α adopts a positive value while β negative.

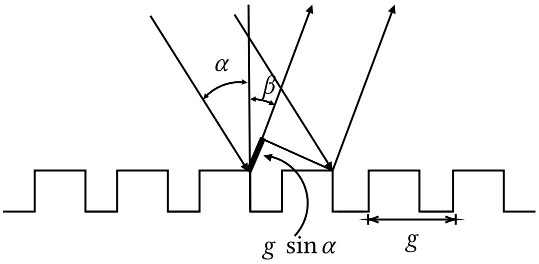

Figure 1: An illustration of a diffraction process from a laminar grating. α and β are angles of incidence and diffraction, g is the period of one grating groove. The sign convention adopted is: α and θ are positive and β is negative.

The periodicity of the grating means that diffracted rays of the same order from adjacent units will be $g\sin\alpha$ out of phase. Constructive interference requires that the path difference be an integer multiple of the wavelength that is of interest. In operation, the user does not usually specify the angles θ (the angle of incidence on the mirror), α, and β independently. The user instead, in the majority of the cases, simply specifies a fixed focus constant (c_{ff}) and an energy, where c_{ff} is defined as:

$$c_{ff} = \frac{\cos\beta}{\cos\alpha}. \tag{2}$$

Along with the desired energy, the angles can be trivially computed. This is known as the fixed c_{ff} mode of operation and is the normal mode of operation. An updated grating equation in terms of only the angle β and c_{ff} can be obtained by algebraic manipulation. Applying the Pythagorean identity to Eq. (2), one obtains:

$$\begin{aligned}\sin^2\alpha &= 1-\cos^2\alpha\\ &= 1-\left(\frac{\cos^2\alpha}{\cos^2\beta}\right)\cos^2\beta\\ &= 1-\frac{\cos^2\beta}{{c_{f\!f}}^2}.\end{aligned} \tag{3}$$

By squaring both sides of Eq. (1) and substituting Eq. (3), one can obtain the updated grating equation:

$$\begin{aligned}\left(\frac{n\lambda}{g}-\sin\beta\right)^2 &= \sin^2\alpha\\ \left(\frac{n\lambda}{g}-\sin\beta\right)^2 &= 1-\frac{\cos^2\beta}{{c_{f\!f}}^2}\\ 1-\left(\frac{n\lambda}{g}-\sin\beta\right)^2 &= \frac{\cos^2\beta}{{c_{f\!f}}^2}.\end{aligned} \tag{4}$$

Eq. (4) is, in essence, a quadratic equation in terms of $\sin\beta$, which can be solved given that all the other parameters are known. α can be computed from β and the specified $c_{f\!f}$. The angle θ is obtained by imposing the constraint that the incoming and outgoing beams must remain parallel, Fig. 2. This gives $2\theta = \alpha - \beta$.

The mechanical evolution of such a setup may be unintuitive. Fig. 2 shows two configurations of the same PGM operating at a fixed $c_{f\!f}$ to give two different energies. By maintaining the same $c_{f\!f}$, a scan over energy is performed by rotating the mirror and grating in a conspired way to effectively change β. Limitations are reached when the beam is no longer incident on the mirror or the grating or the beam footprint becomes too large and flux begins to deteriorate. During the design stage of a PGM, certain geometrical offsets are selected and cannot be altered later. These offsets dictate the essential properties, such as the energy range, as well as its efficiency over said range. Ideally, a set of optimised parameters is chosen. A typical schematic will be presented in Fig. 7 in §2.4.

Eq. (4) also reveals the potential of higher harmonic contamination. For a given set of angles, the PGM will transmit all diffraction orders. This means if a PGM is configured to transmit at 400 eV in the first order, it will also transmit rays with energies that are integer multiples of 400 eV (800, 1200...eV). Furthermore, due to the physics of bending magnets at Diamond, the flux increases with

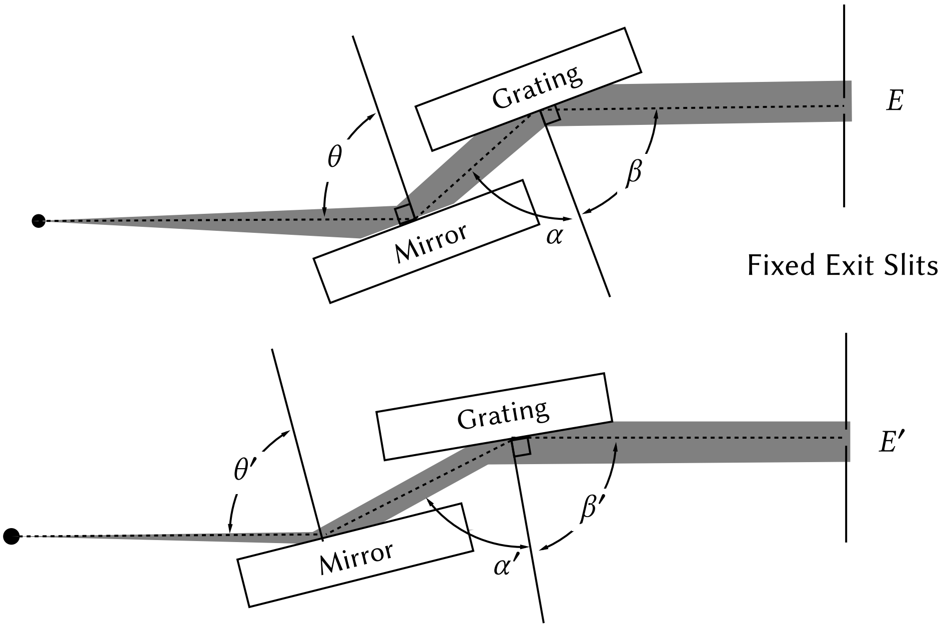

Figure 2: A variation on the popular SX-700 style PGM designed by Petersen *et al.* [13]. Demonstrating the rotations of the mirror and grating to obtain different energies (E and E') in the fixed c_{ff} mode. In the above scenario, $\cos\beta / \cos\alpha = \cos\beta' / \cos\alpha' \equiv c_{ff}$ remains constant; however, $E' > E$. Without loss of generality, $\alpha \neq \alpha'$, $\theta \neq \theta'$, and $\beta \neq \beta'$.

energy in the soft X-ray region [4]. This necessitates ray-tracing over several orders, in addition to the full range of energy and c_{ff} and not just for first order, which is primarily used in order to understand the contribution of higher orders. There is no comprehensive study on the exact impact of higher order contamination in XANES and XAS in general. Physically, one can expect difficulty in the normalisation of the signal; depending on the relative contributions of the different orders, the signal-to-noise ratio could be diminished, possibly losing local information when the sample contains elements with edges which are integer multiples of one another, *i.e.* 2^{nd} order Si K-edge contamination (925 eV in 1^{st} order) when scanning over a Cu L-edge (920-960 eV) [14]. Anecdotal feedback from beamline staff at B07c seems to confirm the presence of higher order contamination. In Fig. 3, the simulated flux spectrum for B07c is presented, with annotated 'H' bars to indicate the intended operational range (first order in red) and the true range of transmitted energies due to higher order contribution (second order in purple and third order in green). The sharp increase in flux with energy in the operational range suggests that contributions from higher order are likely to be significant in the lower energies.

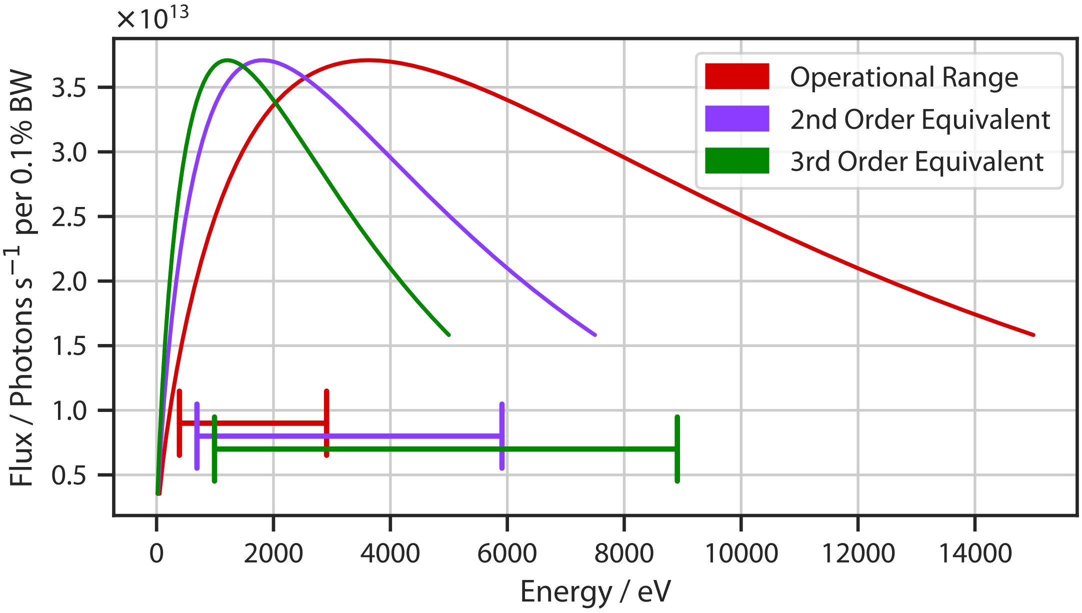

Figure 3: A simulated spectrum of the B07c as calculated by *SPECTRA* [15] (**Red**). The flux is in units of photons per second per 0.1% of bandwidth (BW). 'H' bars indicate the intended operational range (first order in red) and the true range of transmitted energies due to higher order contribution (second order in purple and third order in green)

1.3 Challenges in PGM Ray-Tracing

In this section, current challenges in ray-tracing for PGMs are presented. Discussions, along with the shortcomings of the available methodology, aim to highlight the need for better techniques.

At Diamond and many other synchrotron facilities, the software package *SHADOW* [2] is frequently used to carry out ray-tracing calculations. Currently, *SHADOW* is capable of accounting for both reflectivities of the mirror coating material (common ones include Rh, Si, Pt, *etc.*) as well slope errors, which are imperfections of the optical surface, through its preprocessors *PREREFL* and *WAVINESS*. However, *SHADOW* is incapable of handling geometrical blockages, grating efficiencies, and flux calculations.

The two possible blocking scenarios are presented in Fig. 4, where the beam can be blocked by the physical presence of either the grating or the mirror. By design, *SHADOW* has no *a priori* knowledge of the global optical setup and, therefore, is restricted by the assumption of sequentiality. Due to this design principle of the underlying *SHADOW* codebase, ray-tracing is done in the sequence specified by the user. In normal PGM operation, the correct sequence met by the rays is mirror followed by grating. In both scenarios in Fig. 4, the sequence is broken. Where the rays meet the upstream corner of the grating (Fig. 4 a), *SHADOW* is unaware of the blockage and will transmit 100% of the rays, as formally in *SHADOW*, optical components have no thickness. This is problematic when carrying out simulations for larger energy ranges; *SHADOW* will report an overestimated intensity. This thesis proposes a solution to overcome this fundamental limitation of the software, which will be discussed in §2.

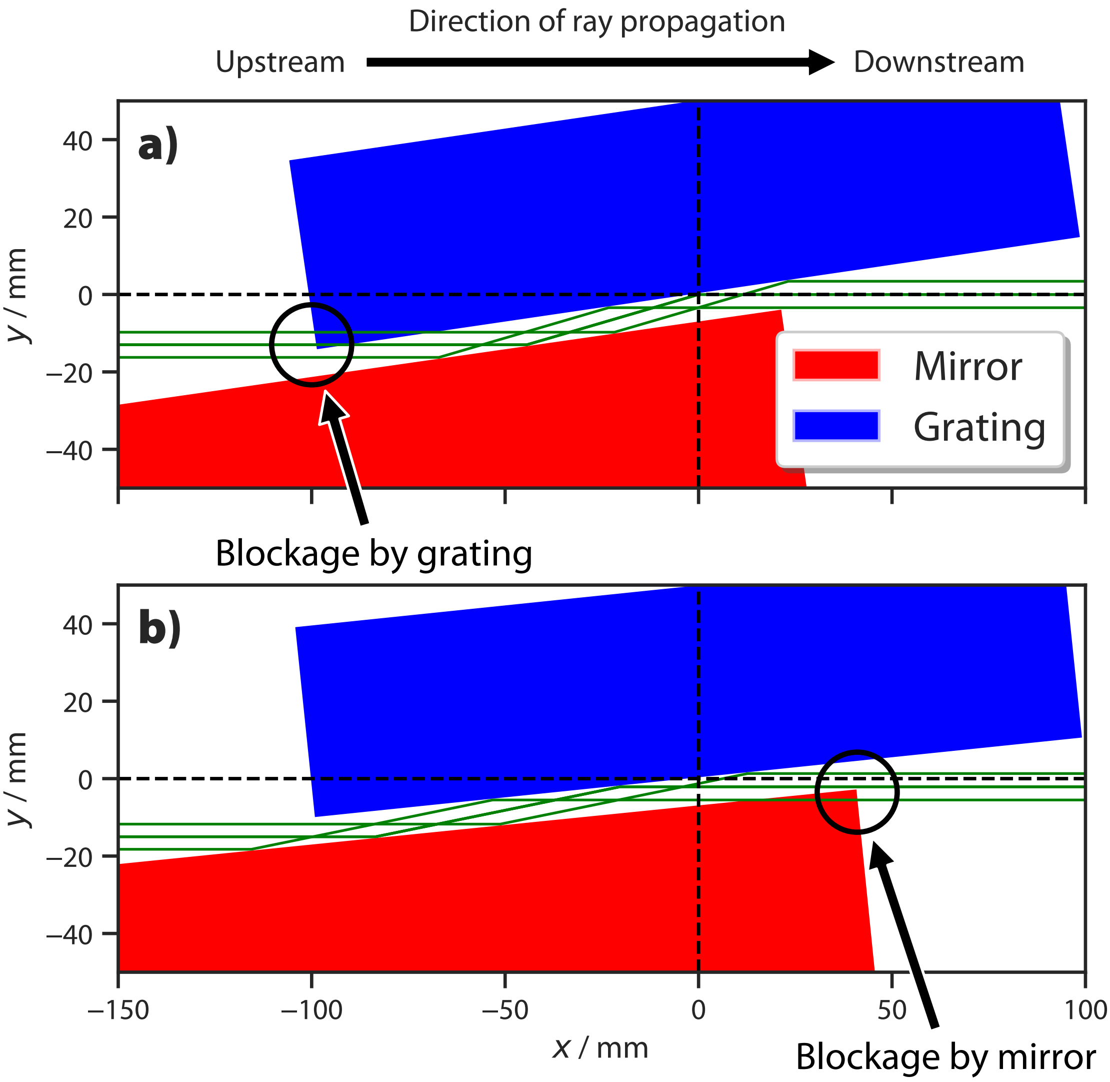

Figure 4: A side view schematic of possible blockages within the PGM during operation. **a)** illustrates partial blockage by the upstream edge of the grating. **b)** illustrates the blockage by the downstream corner of the mirror.

Furthermore, both grating efficiencies and flux calculations have to be handled with packages external to *SHADOW* [15–17]. These calculations present a significant workload where manual adjustments of dozens of parameters are needed. The grating efficiency will vary as a function of both

c_{ff} and diffraction order, as such separate efficiencies must be calculated for each combination of c_{ff} and order. This work can be prohibitive when calculating for several orders, c_{ff}s, and a large energy range. A typical workflow along with a proposed workflow for simulating PGMs is presented in Fig. 5. A full and complete simulation will usually involve performing ray-tracing at the full intended energy range of the PGM over a range of c_{ff}s and several orders, presenting a significant workload, which is why full and complete ray-tracings of PGMs are seldom seen. This thesis presents the programming work that has been completed that enables concurrent calculations for a large number of configurations and different energies. The simulation results can inform a set of optimised c_{ff} settings for the entire energy range, which minimises higher order contaminations and maximises first order flux.

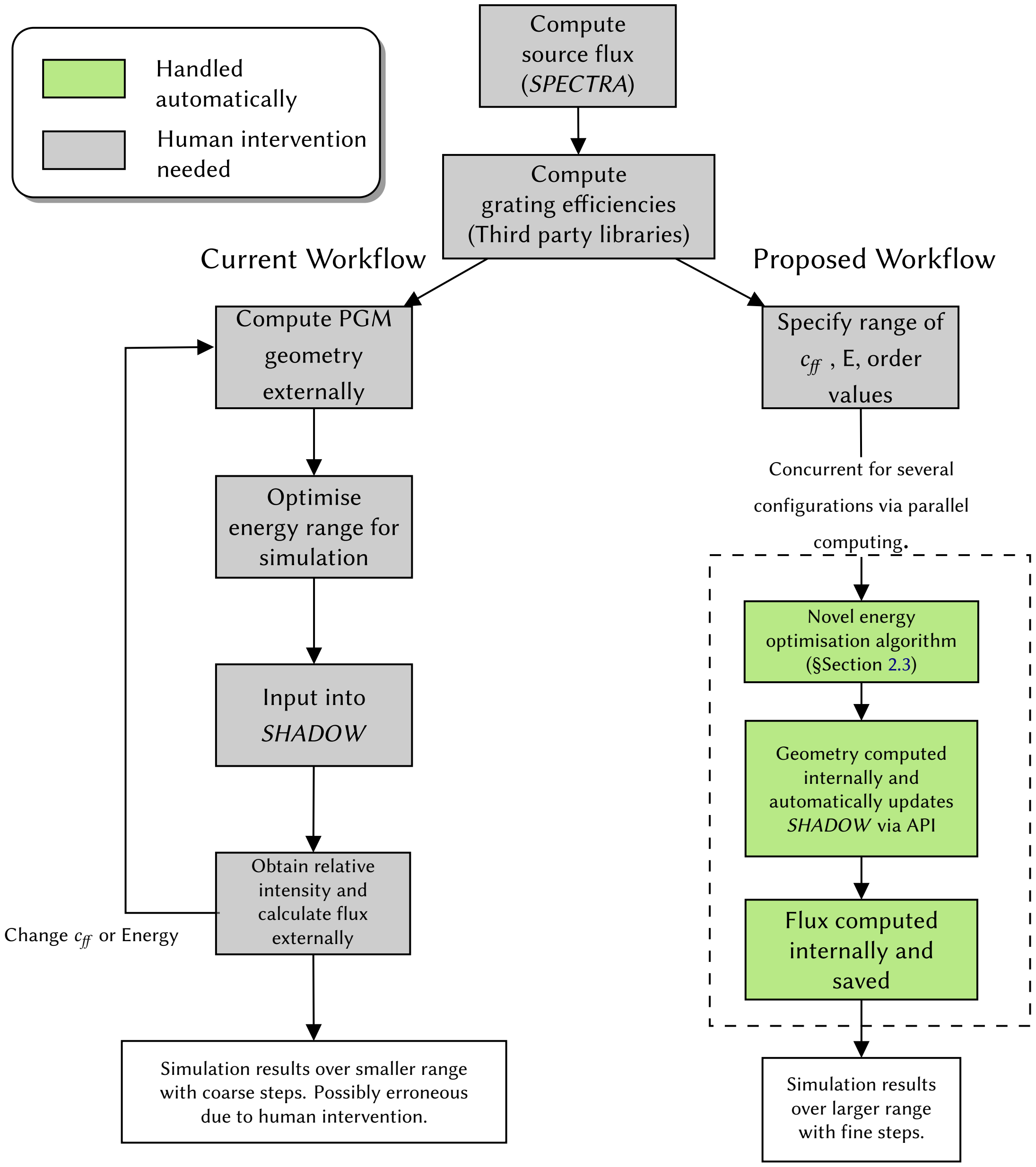

Figure 5: The current and proposed workflow of simulating a beamline with a PGM.

2 Methodology

In this section, a step-by-step account of the proposed workflow is presented sequentially. An introduction to Monte Carlo ray-tracing is given, as it forms an integral part of the work conducted. A more thorough account of the geometrical justifications is presented, as the derivations are fundamental and have not been previously done.

2.1 The Monte Carlo Method and Ray-Tracing

The Monte Carlo method [18] was first proposed by Metropolis and Ulam to be used in the Manhattan Project. This technique has become extremely popular in modern computer simulations involving a large number of particles/events. At its core, the Monte Carlo method replaces deterministic events with probabilities. Via the law of large numbers, by generating a large number of random events and by integration, measurable quantities of the system can be estimated. Mathematically, this data is formalised via the Monte Carlo integration. The probability that the mean of a set of n observations $\bar{u}_n$ of a random variable U is equal to the expected value u approaches 1 as $n \to \infty$:

$$\lim_{n\to\infty} P(|\bar{u}_n - u| < \varepsilon) = 1 \tag{5}$$

where for all $\varepsilon > 0$. Treating an integrable function $f(u)$ as a probability distribution and applying the law of large numbers, one derives the Monte Carlo integration[1]:

$$\lim_{n\to\infty} \left[\frac{1}{n} \sum_{i=1}^{n} f(u_i) \right] = \frac{1}{b-a} \int_a^b f(u)\,\mathrm{d}u \tag{6}$$

where u_i is the i-th number in a set of n randomly chosen values in the interval $[a, b]$ with uniform probability. This calculation results in the transformation of integration into a sum, an operation that modern computers are optimised to perform at a rapid pace. Monte Carlo methods excel particularly in problems involving multidimensional integrations, which include ray-tracing [20].

This idea is incorporated into *SHADOW*, which is one of the primary software packages used in

---

[1] The detailed derivation involves the generalisation from Riemann integration to Stieltjes integration. This is omitted here but can be found in *SHADOW*'s user guide by Cerrina [19].

X-ray ray-tracing of synchrotron radiation. To overcome the prohibitively expensive computational cost of calculating the exact electromagnetic fields and trajectories of a large number of photons emerging from a bending magnet or an undulator, many of which may not have an effect on the final image, *SHADOW* applies a simplified field distribution which can model the radiation properties accurately enough for optical analysis, computing properties such as divergence, beam size. *SHADOW* first computes the source brightness and from it a probability distribution function (PDF) is generated, where the efficient Monte Carlo method can be applied to generate a model of the source [21]. A defined number of rays is then generated by stochastic sampling of the PDF, where the number of occurrences of a ray of particular energy is directly dictated by the PDF. This gives an ensemble of rays whose trajectories and wave vectors can be calculated as they propagate through the optical system, comprised of optical elements (OEs). With each OE, the intensity is attenuated by the optical properties of the OE, *i.e.*, reflectivity, slope error, *etc.* The intensity as returned by *SHADOW* can then be scaled to values of flux simulated by *SPECTRA* [15], which will account for all properties of the machine (bending magnet or insertion device (ID)) as well as the storage ring to give a flux in conventional units.

2.2 Computation of Grating and Mirror Efficiencies

After propagation, be it reflection or diffraction, from each OE, some rays are lost and the intensity is attenuated. For mirrors, reflectivities depend on the electronic properties of the element used in the mirror coating as well as imperfections of the mirror surface (slope errors). These can be computed natively in *SHADOW*, with the preprocessors *PREREFL* and *WAVINESS* respectively. *PREREFL* computes reflectivities by calling the `xraylib` package [22], which is a compilation of previously measured/computed atomic optical constants that can be converted to reflectivity via the Fresnel equations. *WAVINESS* can either calculate lost rays due to specular reflections by using real metrology[2] data or a randomly generated slope error surface.

In the case of gratings, several third-party libraries exist: *REFLEC* [25], *GD-Calc* [16], and *MLgrating* [26]. All produce reliable results that are concordant with each other. The theory involved in the calculation of grating efficiencies is beyond the scope of this work but is presented by Nevière and Popov [27]. In the calculations performed in this thesis for B07c, the grating efficiencies of the 400

---

[2] The science of highly precise measurement of the surface of optical elements using techniques such as interferometry[23, 24].

Table 1: The properties of the B07c gratings used in ray-tracing simulation. Clear aperture describes the size of the grating surface, with tangential being the dimension parallel to the rays, and sagittal perpendicular. c/d is ratio of the height of the laminar groove c to the distance between each groove d.

Property	400 l/mm Grating (Laminar)	Property	600 l/mm Grating (Blazed)
Clear Aperture (tangential × sagittal)	190 mm ×17 mm	Clear Aperture (tangential × sagittal)	190 mm ×30 mm
Coating Material	40 nm of Au	Coating Material	30 nm of Au
Substrate Material	Si	Substrate Material	Si
Line Density	400 lines /mm	Line Density	600 lines / mm
Groove height	11.8 nm	Blaze Angle	0.49°
c/d ratio	0.676	Anti-blaze Angle	175.62°
Aspect angle	7.6°	–	–

and 600 lines/mm gratings are computed using *MLgrating*. The grating efficiency is a function of both the order as well as c_{ff}; consequently, it will require each combination of order and c_{ff} values' efficiency to be computed separately. This was done programmatically by Dr A. Walters [26]. The properties used to calculate grating efficiencies are presented in Table 1.

2.3 Optimising the Simulated Energy Range

Specific to the simulation of PGMs, where scans over energy are essential, the source generation process needs to be optimised. If a PGM is configured with a geometry to transmit 400 eV rays at a particular c_{ff}, the main energy range of interest is significantly smaller compared to the whole operating range of the source. Rays of energies not an integer multiples of 400 eV are not transmitted by the PGM and are therefore wasted. Due to the stochastic nature of *SHADOW*, rays are generated across the source energy. This makes calculation inefficient specifically for the PGM as only rays within a small energy range are transmitted. However, the selected energy range should also not be too small, where it becomes the limiting factor, and thus, the energy resolution ($\Delta E/E$) of the beamline cannot be derived. The appropriate energy range is generally increasing with increasing energy. This thesis proposes a novel iterative algorithm to optimise the simulated energy range. An implementation in `python` is presented:

```python
def optimise(delta_E):
        fwhm = ray_trace(delta_E)
        delta_E_prime = fwhm * 2

        while math.abs(delta_E_prime - delta_E)/delta_E ⩾ 0.3:
```

```
        delta_E = delta_E_prime
        fwhm = ray_trace(delta_E)

        return fwhm * 2
```

where `fwhm` is the full-width half max of the energy histogram after the ray-trace, which is directly related to the energy resolution by a factor of 2. The user would specify an initial `delta_E`, and the iteration continues until the difference between the `delta_E` and the one from the previous iteration converges to within 30%. The optimal `delta_E`, which should not affect the energy resolution information is returned. On average, for an initial `delta_E` of 0.9 eV, the algorithm can optimise the setting within 5 iterations for the energy range 300-3000 eV. Practically, this allows the user to optimise either on the fly before ray-tracing at each step or generate a list of optimised energy settings beforehand and interpolate if necessary as each optimisation only takes a few seconds to converge; compared to previously where the setting is manually applied by the user by mostly guesswork, this provides a faster and more reproducible method for setting up the simulation. An example optimisation run is presented in Fig. 6.

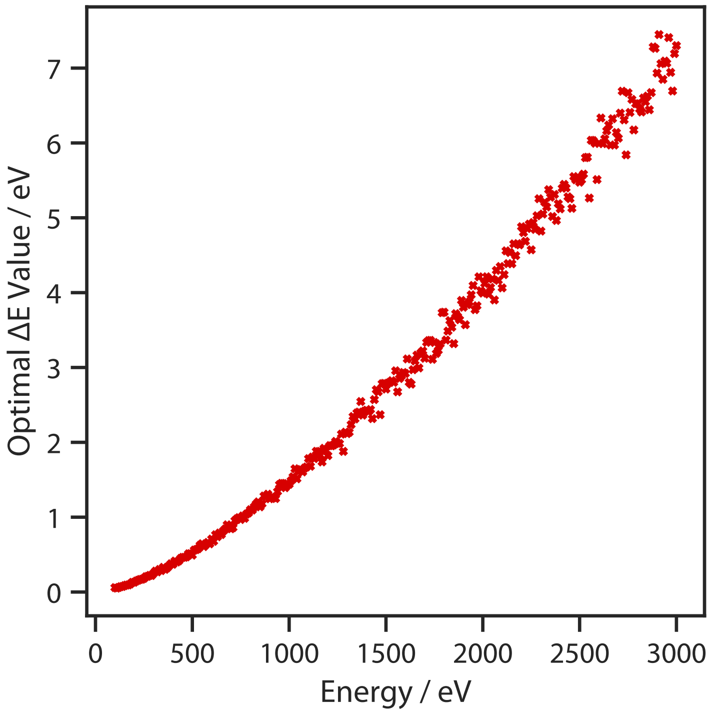

Figure 6: The converged `delta_E` values obtained using the optimisation algorithm for a PGM with c_{ff} = 1.4, 400 l/mm grating in the first order.

In the simulation carried out for B07c, this optimisation is run before each simulation of a different

PGM configuration.

2.4 Geometry of the PGM and input to *SHADOW*

As previously mentioned, one of the primary goals of this work is to be able to correctly account for geometrical blockages of the PGM and accurately simulate it in *SHADOW*. To accomplish this goal, it is important to correctly inform *SHADOW* of the coordinates of the OEs within *SHADOW*'s reference frame.

There are two primary areas of concern: 1. When the incident angle becomes too small, or the beam height becomes too large, the entire beam footprint will not fit on the OE, leading to a loss of flux. 2. Where there are geometrical blockages as illustrated in §Section 1.3. The downstream shadowing requires the correct input of the actual size of the OE into *SHADOW*as well as the location where the beam's centre is incident upon the optical surface. The upstream shadowing requires the introduction of fictitious OEs, which would block any rays that would not have physically been transmitted, unbeknownst to *SHADOW*.

In *SHADOW*, there is no global reference frame as such. Distances and angles of the OEs are defined relative to the OEs that precede them, and the first OE is defined relative to the source. Treating the OEs as planes, one can define the size of the optical surface directly in *SHADOW*. In the context of PGM, this information would simply be the sizes of the mirror and grating, which are known. This input can be easily done by setting the attributes for the appropriate OE. The position of the OE is defined relative to the centre of the beam. A schematic of a modern PGM is presented in Fig. 7, and a written description of the parameters is given in Table 2. By design, the centre of the beam is placed as close to the centre of the grating as possible. Though there will be some small offsets e to $\mathbf{B'}$ from $\mathbf{B}$ in operation, the centre of the beam ($\mathbf{A}$) on the mirror moves significantly in operation.

Table 2: The exhaustive list of parameters that define the geometry of a PGM and the commonly assigned variables. [17]

Description	Parameter Name	Fixed or varying in operation
Location of the centre of beam footprint on the plane mirror	$\mathbf{A}$	Varying
Location of plane grating rotation axis (origin of the x, y coordinate system)	$\mathbf{B}$	Fixed
Location of the centre of beam footprint on the plane grating	$\mathbf{B}'$	Varying
Location of the plane mirror rotation axis	$\mathbf{C}$	Fixed
Location of downstream edge of the plane mirror	$\mathbf{D}$	Varying
Projection of **C** onto plane mirror surface	$\mathbf{E}$	Varying
Location of the bottom left corner of the grating	$\mathbf{G}$	Varying
Distance between **D** and **E**	a	Fixed
Vertical displacement between **B** and incident beam	b	Fixed
Vertical displacement between exit beam and incident beam	b'	Varying
Rotation radius for plane mirror	c	Fixed
Distance between **A** and **B′**	d	Varying
Distance between **B** and **B′**	e	Varying
Vertical displacement between **C** and **B**	v	Fixed
Horizontal displacement between **C** and **B**	h	Fixed
Distance between **A** and **D**	s	Varying

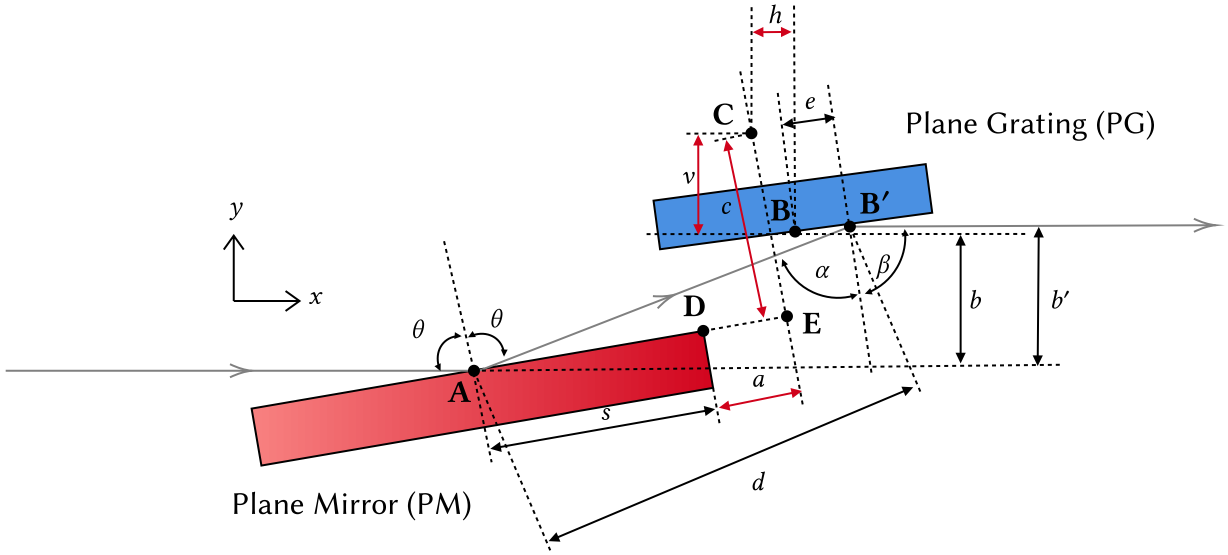

Figure 7: A schematic of a typical modern PGM geometry. Quantities highlighted with red arrows are to be fixed prior to manufacturing. Figure adapted from unpublished work by Dr T.-L. Lee [28].

The derivation of analytical expressions which give the appropriate values for *SHADOW* is presented here. Defining the x axis to be in the direction of the beam propagation (horizontal) and y to be the vertical direction, the grating rotation axis ($\mathbf{B}$) is at the origin $(0, 0)$, which is simply the centre of the grating. The coordinate of the mirror rotation axis ($\mathbf{C}$) is given by h and v, the horizontal and vertical axis offsets: (h, v).

2.4.1 *SHADOW* OE Offsets

It necessarily follows that the projection of the mirror rotation axis C onto the plane of the mirror ($\mathbf{E}$) is given by:

$$\mathbf{E} = \mathbf{C} + c\begin{pmatrix}\cos\theta \\ -\sin\theta\end{pmatrix} \tag{7}$$

and the centre of the beam footprint ($\mathbf{A}$) is given by:

$$\begin{aligned}\mathbf{A} &= \mathbf{E} - (s+a)\begin{pmatrix}\sin\theta \\ \cos\theta\end{pmatrix} \qquad (8)\\ &= \begin{pmatrix}h + c\cos\theta - (s+a)\sin\theta \\ v - c\sin\theta - (s+a)\cos\theta\end{pmatrix} \qquad (9)\end{aligned}$$

where Eq. (9) is the result of combining Eqs. (7) and (8). The vertical component of $\mathbf{A}$ is equal to b, thus equating the corresponding y-component of Eq. (9) allows the centre of the beam footprint's distance to the downstream edge of the mirror (s) to be solved:

$$\begin{aligned} b &= v - c\sin\theta - (s+a)\cos\theta \\ s &= \frac{b + v - c\sin\theta}{\cos\theta} - a \qquad (10)\end{aligned}$$

In *SHADOW*, the position of the centre of the OE is defined relative to the centre of the beam. This position is set via the `OFFY` attribute of the OE. The step to obtain that quantity from s is trivial:

$$\begin{aligned}\Delta y_{\text{mirror}} &= \frac{L}{2} - s \qquad (11)\\ &= \frac{L}{2} + a - \frac{b + v - c\sin\theta}{\cos\theta} \qquad (12)\end{aligned}$$

where L is the length of the mirror. Eq. (12) is the result of rewriting Eq. (11) in terms of quantities that are known as they are either fixed during design (L, a, b, v, c) or calculated given the energy and c_{ff} (θ). It is important to note that this is a vector quantity, where a positive Δy means the displacement of the centre of the OE upwards and negative downwards.

Similarly for the grating, the centre of the beam footprint on the grating ($\mathbf{B}'$) can be expressed either in terms of $\mathbf{A}$ or $\mathbf{B}$:

$$\mathbf{B}' = \mathbf{B} + e \begin{pmatrix} \sin\beta \\ \cos\beta \end{pmatrix} \tag{13}$$

$$\mathbf{B}' = \mathbf{A} + d \begin{pmatrix} \sin 2\theta \\ \cos 2\theta \end{pmatrix} \tag{14}$$

which can be equated with $\mathbf{A}$ substituted by using Eq. (9):

$$\begin{pmatrix} h + c\cos\theta - (s+a)\sin\theta \\ v - c\sin\theta - (s+a)\cos\theta \end{pmatrix} + d \begin{pmatrix} \sin 2\theta \\ \cos 2\theta \end{pmatrix} = e \begin{pmatrix} \sin\beta \\ \cos\beta \end{pmatrix}. \tag{15}$$

Equating the appropriate components allows d to be eliminated:

$$h + c\cos\theta - (s+a)\sin\theta + d\sin 2\theta = e\sin\beta \tag{16}$$

$$v - c\sin\theta - (s+a)\cos\theta + d\cos 2\theta = e\cos\beta. \tag{17}$$

To eliminate d: $\cos 2\theta \times$ Eq. (16) $-$ $\sin 2\theta \times$ Eq. (17) and apply the double angle formula for cos and sin to give a simplified expression

$$e = \frac{(s+a)\cos\theta - c\sin\theta + v\sin 2\theta - h\cos 2\theta}{\sin 2\theta\cos\beta - \cos 2\theta\sin\beta}$$

applying the double angle formula ($\cos 2\theta = 1 - 2\sin^2\theta$) again gives:

$$e = \frac{c\sin\theta - (s+a)\cos\theta - v\sin 2\theta + h\cos 2\theta}{\cos\alpha} \equiv \Delta y_{\text{grating}}. \tag{18}$$

Note that the identity: $\sin 2\theta\cos\beta - \cos 2\theta\sin\beta = -\cos(2\theta - \beta) = -\cos\alpha$ was used[3].

The input of these offsets into *SHADOW*, along with the correct dimensions of the optics, will allow *SHADOW* to natively handle cases where the beam is off partially on the mirror or the grating.

However, enabling *SHADOW* to handle blockages is not trivial. *SHADOW* treats optics as infinitely thin planes with finite sizes (if defined). The blocking fundamentally is a 3D phenomenon which

---

[3] Recall that to ensure the incoming and outgoing beams are parallel, the expression $2\theta = \alpha - \beta$ must be true.

arises because the thickness of the optics is non-zero. To handle this natively in *SHADOW* without extensive modification to the underlying codebase, the following solution is proposed. Two fictitious slits are introduced to the simulated PGM, where the first slit is placed at the upstream corner of the grating and the second is placed at the downstream corner of the mirror. The quantities that need to be known are then:

- the coordinate of the upstream bottom corner of the grating,
- and the coordinate of the downstream corner of the mirror.

The two would simply be used to position the slits to handle the blockages, but the distances from the slits to the next optical elements (`T_IMAGE`) also need to be known. `T_IMAGE` is essential in correctly accounting for the beam size when the beam meets the OEs, as for a beam with non-zero divergence (not collimated), the beam size is either increasing (divergent) or decreasing (convergent) with increasing distance from the source. In actuality, the two parameters that need to be specified for the slits are the offset from the centre of the slit with respect to the centre of the beam and the distance from the slit to the next OE.

2.4.2 Blockage by Grating

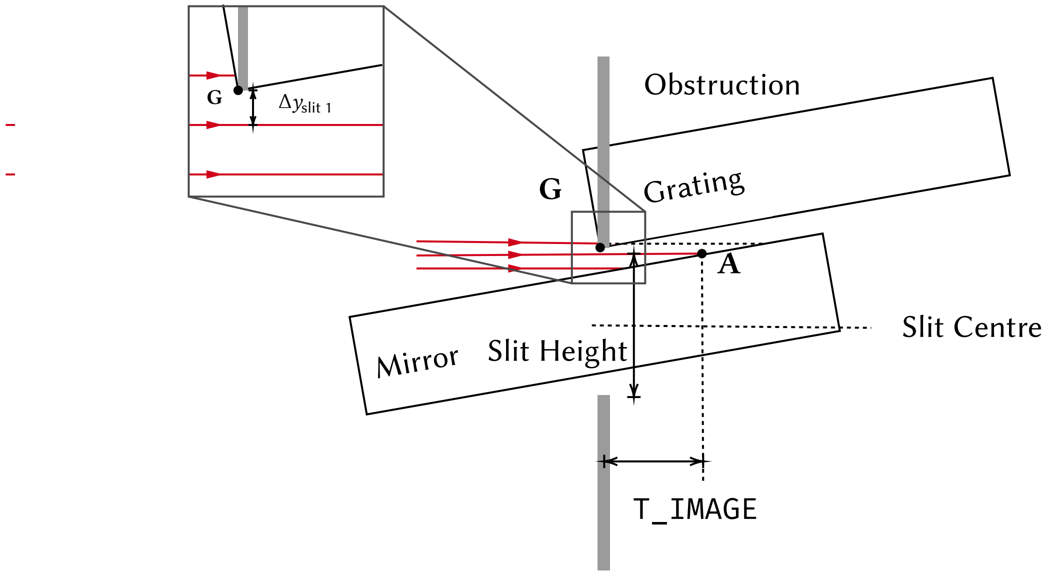

Figure 8: Illustration of the slit positioning in *SHADOW* for blocking by the grating.

A slit is defined in *SHADOW* with a height and the location of the centre of the opening relative to the centre of the beam. To account for blockage by the grating, a slit is introduced in the optical setup as shown in Fig. 8, where we have defined the point **G** to be the bottom left corner of the grating. Programmatically, the slit height is an arbitrary choice, as long as it is set larger than the height of any possible synchrotron beam. The value of 1000 mm was chosen. As illustrated, the slit should be translated down such that the bottom of the upper obstruction is placed at **G**. The quantity of interest is hence the distance from the centre of the beam to **G**, which is denoted as $\Delta y_{\text{slit 1}}$. **G** can be expressed as:

$$\mathbf{G} = \frac{l}{2}\begin{pmatrix} \sin\beta \\ -\cos\beta \end{pmatrix} \tag{19}$$

where l is the length of the grating. An expression for Δy_1 can then be derived:

$$\Delta y_{\text{slit 1}} = A_y - G_y = v - c\sin\theta - (s+a)\cos\theta + \frac{l}{2}\cos\beta \tag{20}$$

where A_y and G_y are the y components of the points **A** and **G** respectively. A_y is substituted using Eq. (9). The `T_IMAGE` parameter is then the horizontal distance from **G** to **A**:

$$\texttt{T\_IMAGE} = A_x - G_x = h + c\cos\theta - (s+a)\sin\theta - \frac{l}{2}\sin\beta \tag{21}$$

2.4.3 Blockage by Mirror

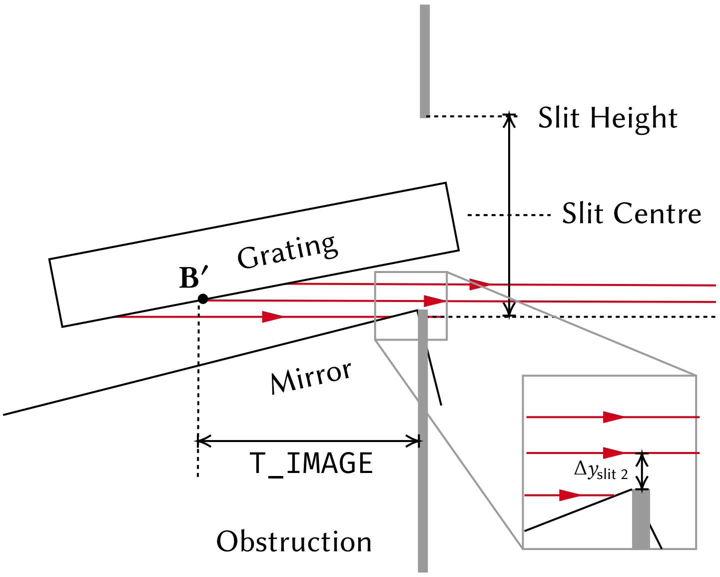

Figure 9: Illustration of the slit positioning in *SHADOW* for blocking by the mirror. The distance from the corner of the mirror to the central beam in the illustration is the vertical distance from the corner to an extension of **B′**.

Similarly, for the blockage by mirror, the coordinate of the downstream mirror corner ($\mathbf{D}$) needs to be known. Once again, this is relative to the centre of the beam $\mathbf{B}'$, Fig. 9.

From Eq. (13), the x and y components of $\mathbf{B}'$ can be extracted:

$$B'_x = e\cos\beta \equiv \Delta y_{\text{grating}} \tag{22}$$

$$B'_y = e\sin\beta \equiv \Delta y_{\text{grating}} \tag{23}$$

The required offsets are once again the horizontal and vertical distances from the two points:

$$\begin{aligned} \Delta y_{\text{slit 2}} &= B'_x - D_x \\ &= \Delta y_{\text{grating}}\cos\beta - \left(-\frac{c}{\sin\theta} + (a - c\cot\theta)\cos\theta + v\right) \qquad (24) \\ \texttt{T\_IMAGE} &= B'_z - D_z \\ &= \Delta y_{\text{grating}}\sin\beta - (h - [(a - c\cot\theta)\sin\theta]) \qquad (25) \end{aligned}$$

It is important to note that the `T_IMAGE` for the second slit is not a property of the slit but a property of the grating OE, as in *SHADOW*, the OEs are defined relative to the previous OE. Thus, the ray-trace sequence for the PGM is:

1. Slit 1, to handle blockage by the upstream edge of the grating. Defined by $\Delta y_{\text{slit 1}}$ and `T_IMAGE` (distance to the mirror).
2. Mirror, to deflect the rays to meet the grating. Defined by Δy_{mirror} and `T_IMAGE` (distance to the grating).
3. Grating, to disperse the rays in energies. Defined by $\Delta y_{\text{grating}}$ and `T_IMAGE` (distance to slit 2).
4. Slit 2, to handle the blockage by the downstream corner of the mirror. Defined by $\Delta y_{\text{slit 2}}$.

All the parameters which are needed to specify a PGM in *SHADOW* are known:

- Sizes of the OEs
- Angles of incidence and diffraction (§1.2)

- Mirror and grating efficiencies
- Mirror and grating translations relative to the beam (Δy_{mirror} and $\Delta y_{\text{grating}}$)
- Position of the slits

All the calculations are compiled into callable functions in a `python` library and is available on GitHub as well as its extensive documentation. This package is meant to complement *SHADOW* and act as a *de facto* pre-processor. The code was used in the extensive ray-tracing simulation for beamline B07c.

2.5 Simulation for B07c and Parallelisation

The primary goal is to be able to simulate the behaviour of a PGM over a large energy and c_{ff} range. Iterations are unavoidable. Despite the fact the *SHADOW* is already very performant, iteration in `python` can be slow. For the work carried out for B07c, the calculation involved simulating the PGM from energies 300 to 15000 eV in 10 eV steps, c_{ff} from 1.05 to 3.0 with uneven step sizes, and for all orders one through five. Multiprocessing was introduced by using the built-in `python` library. This allowed parallel computation and reduced the simulation time drastically. For the complete simulation of B07c, the calculation ran for no more than 10 hours on a consumer-grade machine.

Calculations were carried out for the B07c beamline, Fig. 10. All mirrors except for M2c in the beamline are coated with rhodium. M2c, the PGM mirror can be chosen between two stripes of platinum, and rhodium. The beamline primarily uses the platinum-coated section of the mirror, but calculations were carried out for both. In addition, the In simulation, the exit slits are fixed to be 100 microns, in reality, this would be adjusted to cater to the required energy resolution, with a smaller slit size yielding a higher energy resolution.

With these calculations, the most efficient combination of a c_{ff}setting at different energies can be investigated. This can inform the beamline users on deciding how to best achieve what is needed for their experiment. Furthermore, the simulations can be used to optimise future beamline designs.

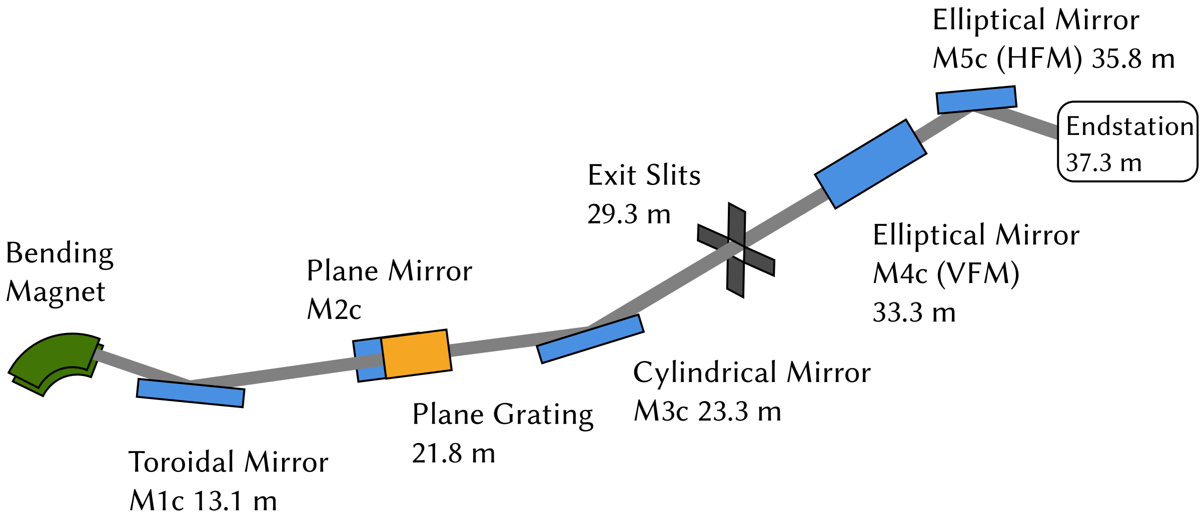

Figure 10: The layout of the simulated beamline B07c, figure adapted from [5]. The PGM is formed by M2c and the Plane Grating. Acronyms used:vertically focusing mirror (VFM) and horizontally focusing mirror (HFM). Distances are given in meters from the centre of the optic to the bending magnet source.

3 Results and Discussion

In this section, results from the preliminary test ray-tracings are presented to establish the validity of the methodology, followed by the ray-tracing results for B07c. Calculations were carried out for two of the possible combinations of optics: platinum PGM mirror with 400 l/mm grating, and platinum PGM mirror with 600 l/mm grating. Both gratings are gold coated. Energies ranged from 300 eV to 3000 eV for the first order, up to 6000 eV for the second order, 9000 for the third, 12000 for the fourth, and 15000 for the fifth. A simultaneous scan over c_{ff} was performed from 1.05 to 3.0 with uneven step sizes. Finer sampling is necessary at lower c_{ff}s due to the design of the PGM, which will be discussed in due course. A figure of merit (FoM) function is suggested, which should, in theory, provide a meaningful tool for the beamline to easily determine the best c_{ff}-energy combination to operate at to maximise flux and minimise higher order contamination.

3.1 Validating the Methodology

As with any newly developed methodology, one needs to confirm if it produces physically sensible results. Results here are presented for the platinum PGM mirror and 400 l/mm grating combination. First, to verify that the blocking has been implemented correctly, a *transfer function* as a diagnosis tool is proposed.

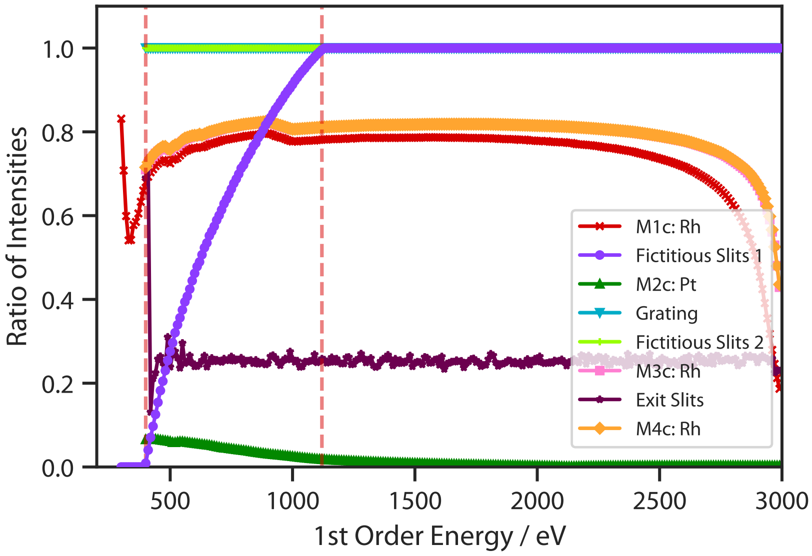

Figure 11: The proposed transfer function plot for B07c PGM with the Pt mirror and 400 l/mm grating at $c_{ff} = 1.05$. Note the increasing behaviour of Fictitious Slits 1 (purple) between the dashed lines at energies 300 and 1120 eV.

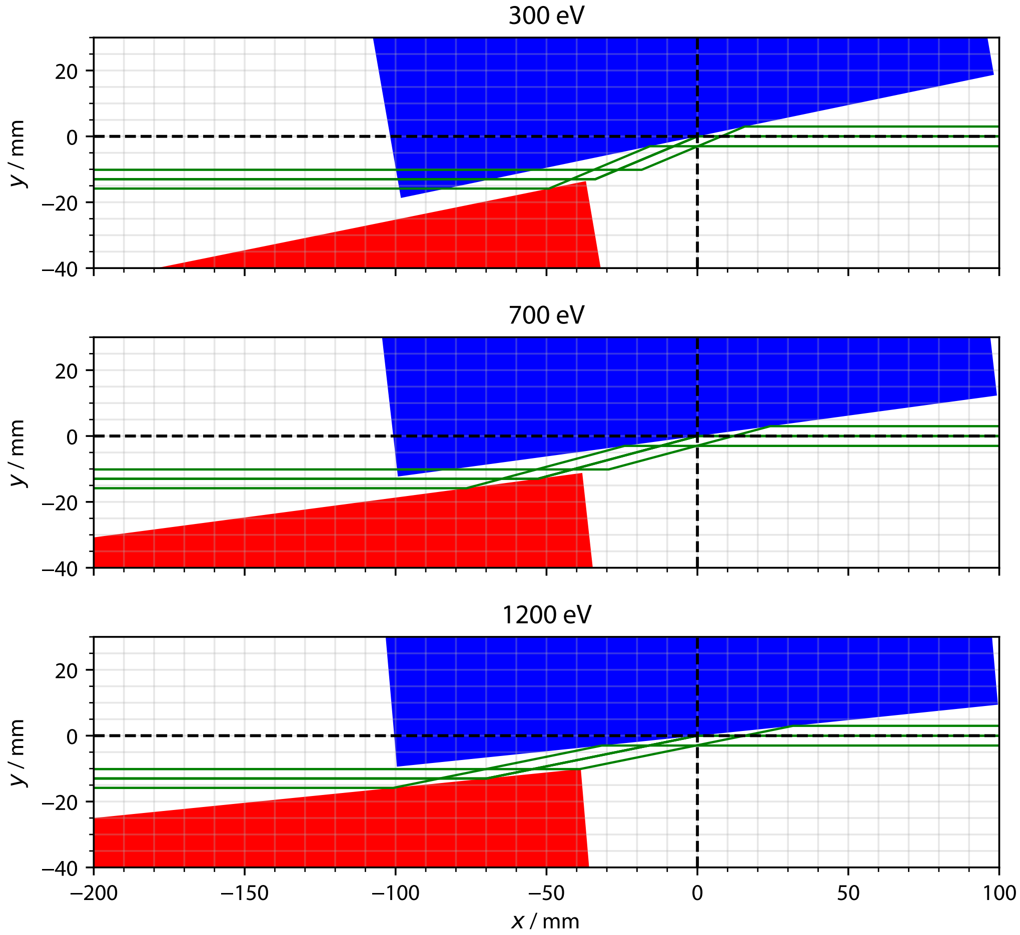

Figure 12: The B07c PGM at c_{ff} of 1.05 at three different energies: 300, 700, and 1200 eV. Complete blocking at 300 eV, partial at 700 eV, and no blocking at 1200 eV.

For validation, the number of rays as well as the total intensity after each OE is stored. The intensity being the magnitude of the electric ($\mathbf{E}$) and magnetic ($\mathbf{B}$) fields summed in quadrature ($\sqrt{|\mathbf{E}|^2 + |\mathbf{B}|^2}$). The transfer function plots the relative ratios of the intensities between two adjacent OEs, *i.e.* M1c/Bending Magnet, Fictitious slit 1/M1c... as a function of energy. This will isolate the effect of the OE in question and allow visualisation of its effect and its effect alone, highlighting isolated effects that are energy dependent, *i.e.* geometrical and reflectivity related. An example of this is observed for M1c, a rhodium mirror, exhibits lower reflectivity above the rhodium *L*-edge (E > 2800 eV). For the B07c PGM, if operated at $c_{ff} = 1.05$, blockage by the grating will occur. The transfer function is presented in 11 with side view diagrams shown in Fig. 12.

The aforementioned transfer function should show that the relative intensity at the first slits is zero below ca. 300 eV and increases until unity at ca. 1200 eV. This is presented in Fig. 11. The increasing behaviour is present, and the ratio reaches 1 at ca. 1120 eV. The falloff in intensity is observed for M4c, M3c, and M1c, which are all rhodium mirrors, at ca. 3000 eV, which corresponds to the rhodium L-III edge at 3004 eV [14]. Due to the large angle of incidence at this c_{ff}, the efficiency of the platinum mirror has deteriorated so much that the absorption edge can not be identified in this plot. Typically, high normal incidence reflectivity of mirrors can only be realistically achieved for light with energy in the visible and UV region. In soft X-ray applications, the angle of incidence (relative to the normal) must be as close to 90° as possible to maintain maximum reflectivity [29]. Because of the energy optimisation step previously introduced, the exit slits ratio remains constant; the stochasticity is from the optimisation algorithm, which was represented by the scatter in Fig. 6 in §2.3.

However, at a more plausible c_{ff} of 1.4, which the beamline does operate at, the platinum M-edge (2122 eV [14]) absorption edge can be clearly identified, Fig. 13. The gold coating of the grating has absorption edges closely overlapping with that of platinum, as they are adjacent on the periodic table.

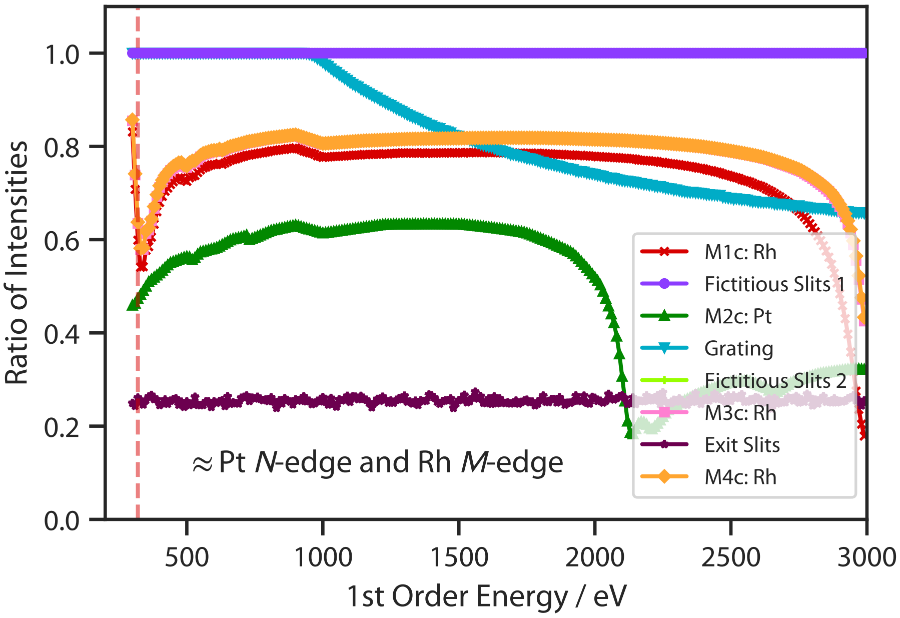

Figure 13: The proposed transfer function plot for B07c PGM with the Pt mirror and 400 l/mm grating at $c_{ff} = 1.4$. Note no blockage occurs and slits transmit 100% of the rays. The fall-off of the grating ratio starting at ca. 1000 eV is due to the over-illumination of the grating Fig. 14. The dotted red vertical line is at 320 eV, which corresponds to Pt N-edge and Rh M-edge absorptions.

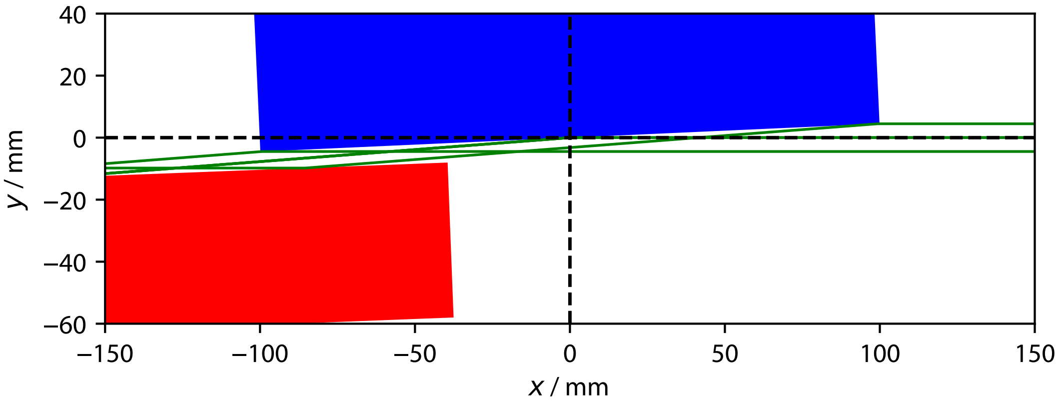

Figure 14: B07c PGM side-view at $c_{ff} = 1.4$, 1000 eV, where the beam footprint is becoming too large for the grating. The beam height drawn is 6.38 mm, as calculated by *SHADOW* for this energy.

The fall-off of the grating ratio is observed to start at just below 1000 eV (blue line in Fig. 13). This can be explained by the fact that the grating is over-illuminated, causing the flux to deteriorate, Fig. 14.

The transfer function plots also highlighted the deficiencies of currently used optical constants in *SHADOW*. The observed unphysical ‘steps’ present in both Figs. 11 and 13 at just below 1000 eV is an artefact present in `xraylib`, the database used to obtain the optical constants to compute the reflectivities. `xraylib` itself uses a database compiled by Elam and colleagues [30]. The database was primarily composed of scattering constants measured by Berger and Hubbell [31] from 1 keV upwards, and Plechaty *et al.* below 1 keV [32]. To connect the datasets smoothly, Elam *et al.* performed linear interpolation, which leads to the artefact that is observed on the transfer function plots. This highlights a deficiency in *SHADOW*’s capabilities in the soft X-ray range. Contrary to the hard X-ray region where optical constants are well measured and values from different publications are in good agreement, optical constants in the soft X-ray region are poorly tabulated due to the difficulty in measuring them. This thesis makes the recommendation of adopting the values reported by Henke *et al.* [33], which contains optical constants over the complete energy range of interest in the soft X-ray range, for future simulations.

3.2 Higher Order Contribution to the Flux

The transfer function plot proved to be a very useful diagnostic tool which can provide large amounts of information about the physics that is encapsulated. To better understand the beamline performance, further flux calculations were carried out, which involved scaling the final intensity after M5c by the simulated flux from *SPECTRA* and scaling to the correct bandwidth. The fluxes of orders 1 to 5 for the two primary c_{ff}s, which the beamline operates at, 1.4 and 2.0, are presented in Fig. 15. This allows the study of the theoretical flux that can be used for experiments. As previously described, given a set geometry, a PGM will transmit integer multiples of the first order energy, hence higher order fluxes (up to 5th) are included in all simulations. The energies of the higher order simulations are scaled to 'first order energy' to emphasise that it is the PGM setting at which the higher orders will be transmitted. In Fig. 15 a) and b), the absorption edges of rhodium and platinum can be observed, with edges in the higher order scaled appropriately, *i.e.*, a second order absorption edge at 3000 eV is plotted as 1500 eV in the graph as first order energy.

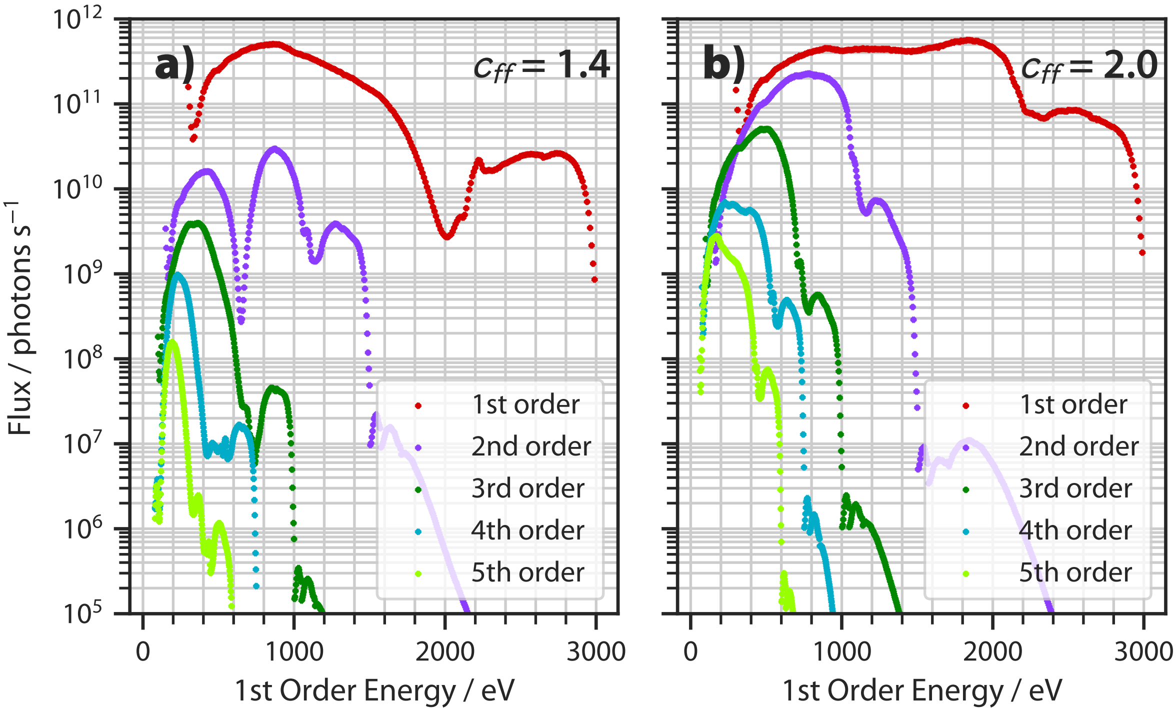

Figure 15: **a)** Flux simulations carried out for orders 1-5 at c_{ff}=1.4, and **b)** at c_{ff}=2.0. Both are for the B07c Pt mirror and 400 l/mm grating combination. Note that the x-axis plots **first order energy**, *i.e.*, real energy / order. 600 eV at second order is plotted as 300 eV in first order energy as those rays are transmitted with the same PGM geometry.

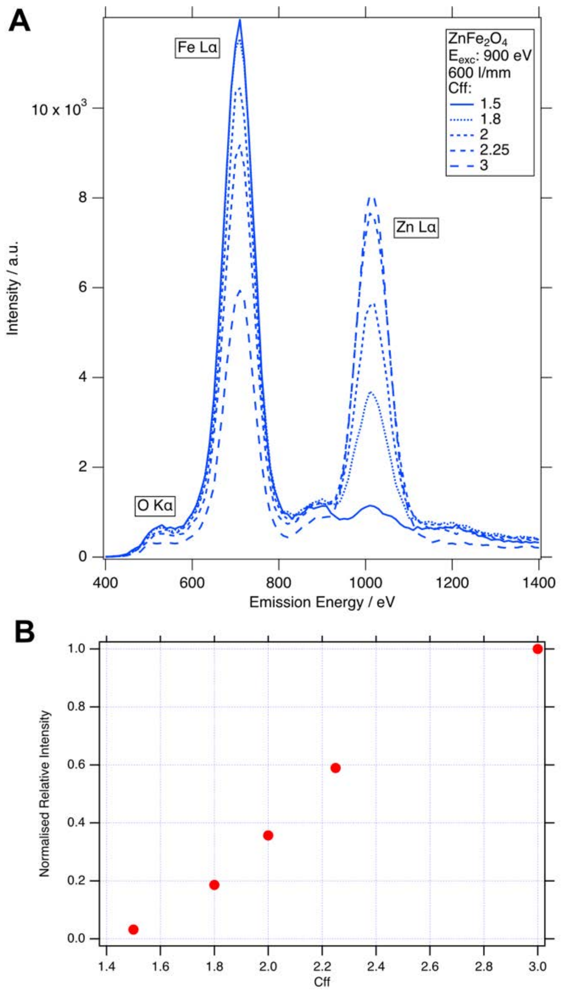

Figure 16: **A**:XES measurement of $ZnFe_2O_4$ at various c_{ff} values set to 900 eV at B07**b**. Figure reproduced from work by Grinter *et al.* [34] Emission from excitations of Fe L-edges (706-720 eV [35]) is clearly visible, in addition to emission by Zn's L-edge at 1021 eV [14]. **B**: the normalised intensity of the Zn $L\alpha$ edge labelled in A as a function of c_{ff}.

The simulation results for the 400 l/mm grating at a c_{ff} of 2.0 shown in Fig. 15 b). For energies below 1000 eV, the flux from the second order is comparable to that of the first. This would suggest significant higher order contamination, which is supported by anecdotal evidence from beamline staff. Though not the same beamline, B07b (a second branch of B07) uses a PGM whose configuration is very similar to that of B07c. Direct X-ray emission spectroscopy (XES) measurements of zinc ferrite ($ZnFe_2O_4$) confirms the presence of second order contamination. This is seen in the XES data presented in Fig. 16A. A series of emission spectra of $ZnFe_2O_4$ is obtained by fixing the PGM energy to be 900 eV and scanning c_{ff} values from 1.5 to 3.0. In Fig. 16A, the intensity of emission signal from the $L\alpha$ edge at 720 eV increases with decreasing c_{ff} values. The opposite is true for the Zn $L\alpha$ edge at ca. 1040 eV. Fig. 16B shows the Zn peak heights relative to the peak height at c_{ff}=3.0. The excitation of Zn should be absent as higher energies above 900 eV should have been filtered by the PGM.

Furthermore in Fig. 15, it is observed that with increasing order, the flux decreases. Though the spectrum of the bending magnet produces higher flux at higher energy (up to 4000 eV for B07c), the grating efficiency at higher orders is quickly deteriorating. This means that despite the advantage higher orders have from the bending magnet source, they are suppressed by the grating significantly. Despite this benefit, second order still contributes appreciably for the higher c_{ff}.

For B07c at c_{ff}=2.0, the transmitted higher order fluxes are of equal magnitude to first order, at times surpassing first order flux (ca. up to 500 eV for c_{ff} 2.0.)

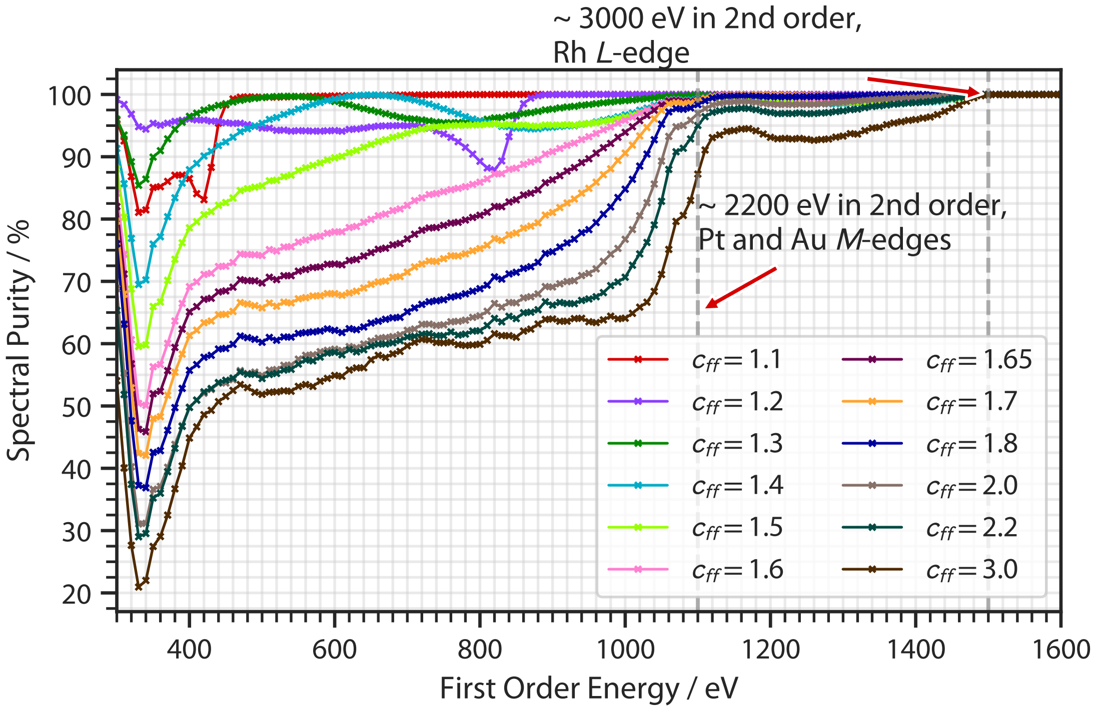

Figure 17: The spectral purities of the beam after the final OE in the Pt and 400 l/mm mirror-grating combination as a function of energy. Gray dotted lines at 1100 and 1500 eV in first order energy, corresponding to absorption edges in the second order at 2200 eV and 3000 eV.

Simulation at other c_{ff}s indicates a general trend of increased contamination with increasing c_{ff}. Here, to compare the performance between different values of c_{ff}, the spectral purity as a measure is defined:

$$\text{Spectral Purity} = \frac{\text{First order Flux}}{\text{Total Flux}} \times 100\%. \tag{26}$$

The contribution of first order flux should ideally be as close to 100% of the total flux. A selection of spectral purities at different c_{ff}s is plotted in Fig. 17.

The deterioration of the spectral purity from c_{ff}=1.1 to 1.8 is much more rapid compared to higher c_{ff}s, where the spectral purity seems to be slowly plateauing at ca. 60% up to 1100 eV. The stagnation of the decrease in spectral purity can be explained by the fact that the angles are changing much more drastically as a function of c_{ff} at lower c_{ff}s than higher ones, Fig. 18. This results in the rapid change of behaviour with changing c_{ff} at low c_{ff} values, as the angles are evolving quickly, consequentially changing the reflectivity of the optics.

Drastic and systematic improvements to the purity across all c_{ff}s are observed at 1100 eV and 1500

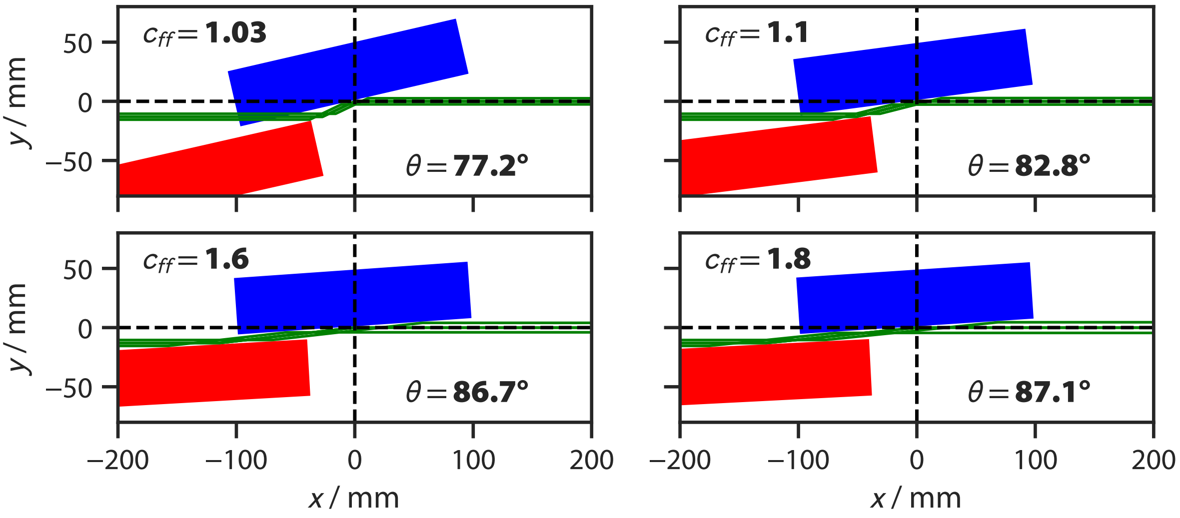

Figure 18: A series of side-view diagrams of the B07c PGM for c_{ff}s of 1.03, 1.1, 1.6, 1.8 at a fixed energy of 500 eV along with the angles of incidence on the mirror (θ). This is an illustrative selection only to demonstrate the evolving geometry of the PGM. Note that the angle change at lower c_{ff}s is significantly more pronounced.

eV. The first improvement can be accounted for by the absorption edges of Pt and Au on the mirror and the grating at 2200 eV (1100 eV in first order energy), greatly suppressing the transmission of higher order flux. Similarly for the improvement at 1500 eV with Rh L-edge absorption [14]. The mirrors and grating acted as a *de facto* low pass filter; as the desired first order energy is 1100 eV, which is below the absorption edges, and is subsequently transmitted. All higher orders are suppressed. Fig. 15 b) shows that the majority of the contamination at c_{ff}=2.0 comes from the second order from 250 to 400 eV, and third order from 75 to 250 eV, which unfortunately, lie below the absorption edges. The low pass filter property of the mirror optic was previously exploited to build a higher order suppressor [36, 37]. Beamline B07c operates a collimated PGM scheme, where the incoming beam has zero vertical divergence at the PGM. This carries the benefit of being able to choose the c_{ff} freely for a given energy, as the beamline does not need to rely on any focussing properties of the grating [26].

This motivates the search for an energy-c_{ff} combination which maximises first order flux and suppresses higher order flux. The individual effect per order is presented in Fig. 19. For easier association, a set of conventional colours have been chosen for the different orders and are maintained for all subsequent plots.

From Fig. 19, one observes that the second order contributes significantly more than the third and fourth order. The same suppression at the Pt and Rh absorption edges are once again observed for the first and second order, Fig. 19a) and b). In the range of 300 eV to ca. 1500 eV, suppression of second order is especially poor, with contamination above 25%. This is problematic, as this is the beamline's core energy range. Their choice of operating at a c_{ff} of 1.4 can be fully justified, as it can be seen in Fig. 19 a) that a c_{ff} value of 1.4 resides just at the lower edge of the region of high flux in addition to the upper edge of low second order contamination.

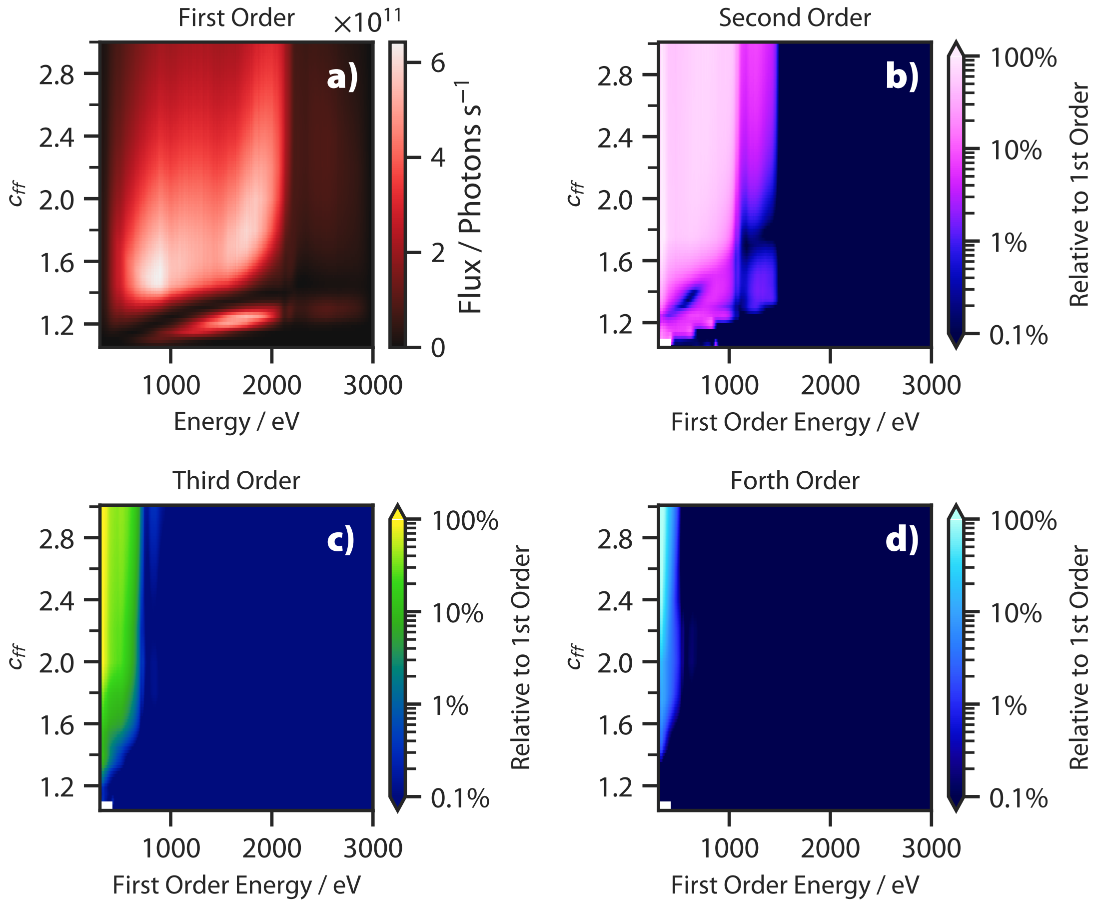

Figure 19: Results for the 400 l/mm grating presented as four heat maps of **a)** first order flux as a function of c_{ff} and energy; **b), c), d)** second, third, and fourth order flux relative to the first order flux as a function of c_{ff} and first order energy. Note the logarithmically scaled colour bars. 2D linear interpolation is applied to all four datasets.

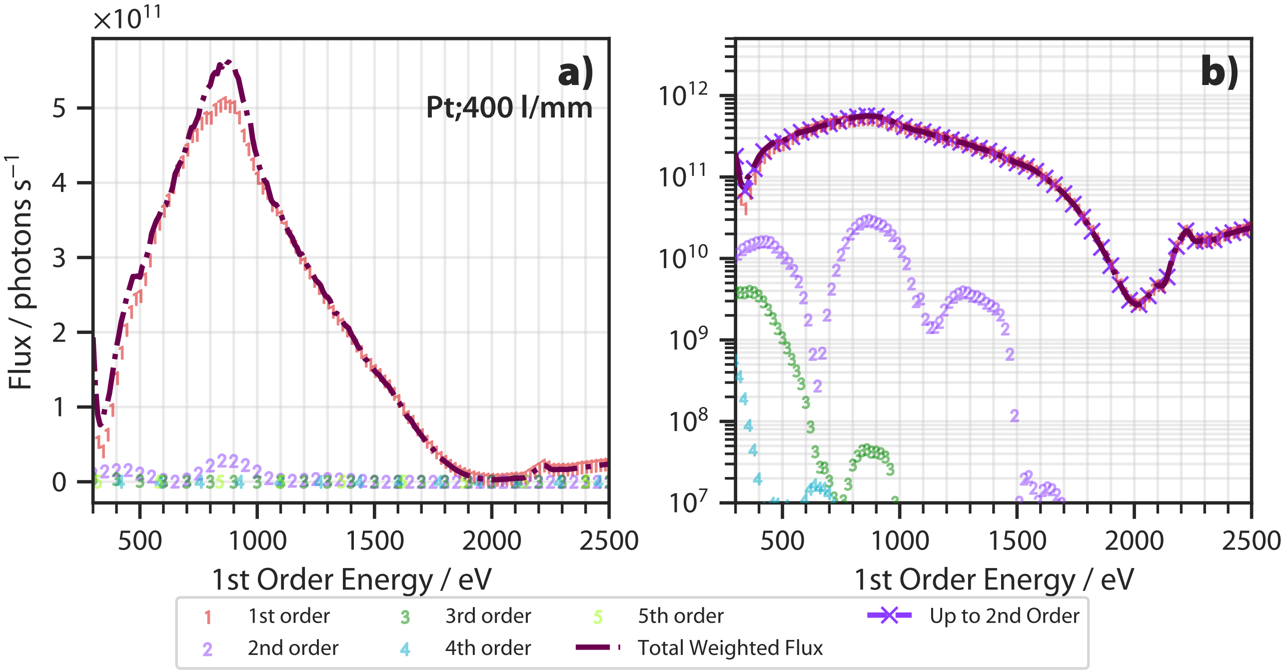

Figure 20: **a)** Simulation results for 400 l/mm grating PGM at c_{ff}=1.40. **b)** the same data plotted on a log y-axis as well as summed flux of first and second order.

The contribution from higher orders can be further examined by a combination plot, Fig. 20. In **a)**, the fluxes are plotted along with *total weighted flux.* In practice, the flux measuring devices which are used have sensitivities that are functions of energy. B07c uses a photodiode, which is doubly more sensitive to the second order than the first, and likewise for higher orders. Here, the weighted flux as a quantity is introduced:

$$\text{Weighted Flux} = \sum_{i \in \{\text{orders}\}} i \times F_i(E_{1^{\text{st}}\ \text{Order}}) \tag{27}$$

where $F_i(E_{1^{\text{st}}\ \text{Order}})$ is the flux of the i-th order at first order energy. The total weighted flux is then the total transmitted flux of all orders given a PGM geometry. This gives a useful metric, as it more closely resembles what the beamline can measure. The low c_{ff} value of 1.4 does indeed contain little higher order contamination without overly sacrificing the total flux. In contrast, however, the same plot is presented for c_{ff}=2.0 in Fig. 21. The total weighted flux is significantly higher, almost double that at 1.4, but the contribution from higher orders accounts for 50% of the total weighted flux as measured by a photodiode in the lower energies.

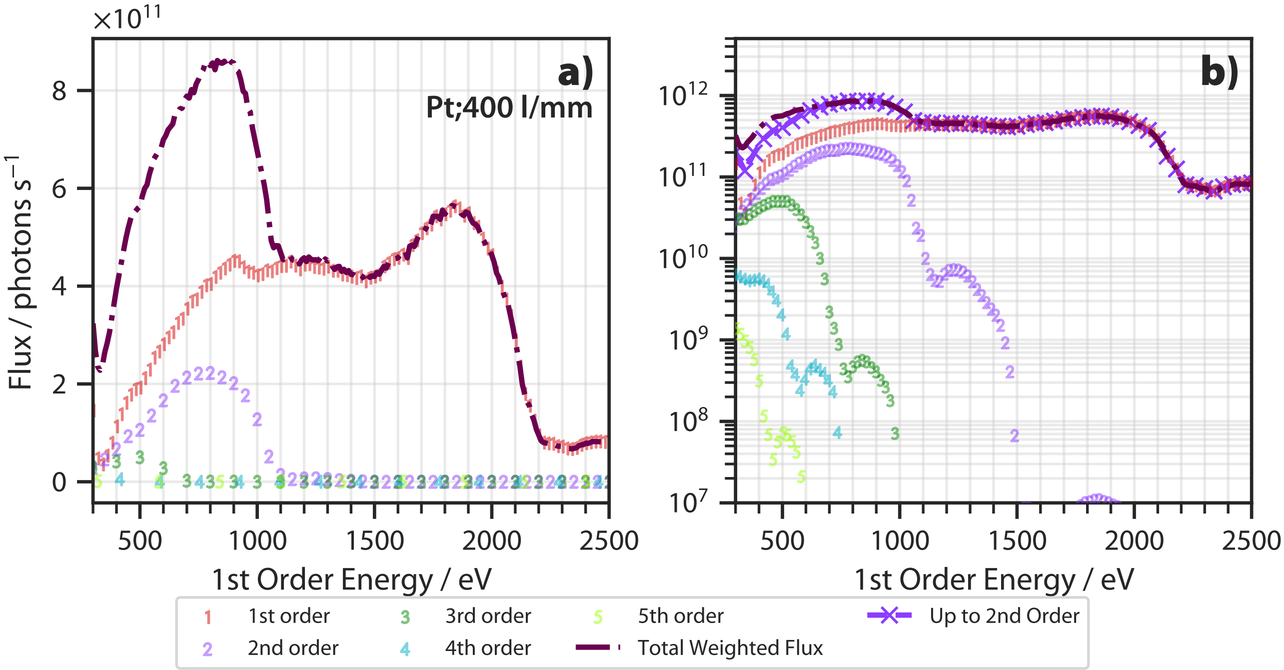

Figure 21: **a)** Simulation results for 400 l/mm grating PGM at c_{ff}=2.0. **b)** the same data plotted on a log y-axis as well as summed flux of first and second order.

In the other configuration with 600 l/mm grating, the higher order contamination is discernibly less prominent compared to the 400 l/mm grating, Figs. 22 and 23. Again, second order contributes primarily in the lower energy range of 500-1100 eV. The total flux is generally comparable but for a c_{ff} value of 2.0, the first order flux for the 400 l/mm grating is less than half of the total weighted flux, compared to 600 l/mm where the first order is ca. 70% of the total flux at 1000 eV. In addition, the peak flux of the 600 l/mm grating is at ca. 1500 eV and is roughly twice that offered by the 400 l/mm grating at 800 eV. The higher order suppression quality of the blazed grating (600 l/mm) [38] is thoroughly demonstrated here. Though in these two instances of c_{ff} and considerations of purely maximising first order flux. It as apparent that the 600 l/mm grating outperforms the 400 l/mm grating by a wide margin. The immediately obvious optimisation would be to use the 600 l/mm grating in all instances where the desired energy is above ca. 500 eV. A detailed analysis on the suggested mode of operation is to follow.

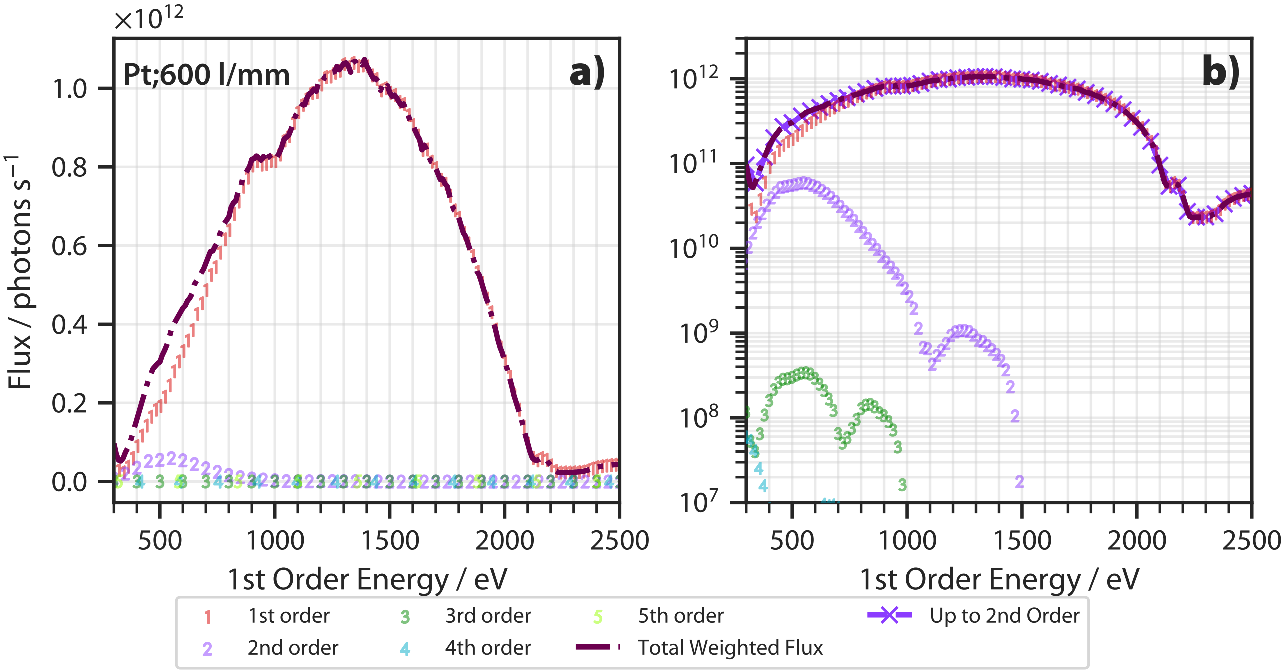

Figure 22: **a)** Simulation results for 600 l/mm grating PGM at c_{ff}=1.4. **b)** the same data plotted on a log y-axis as well as summed flux of first and second order.

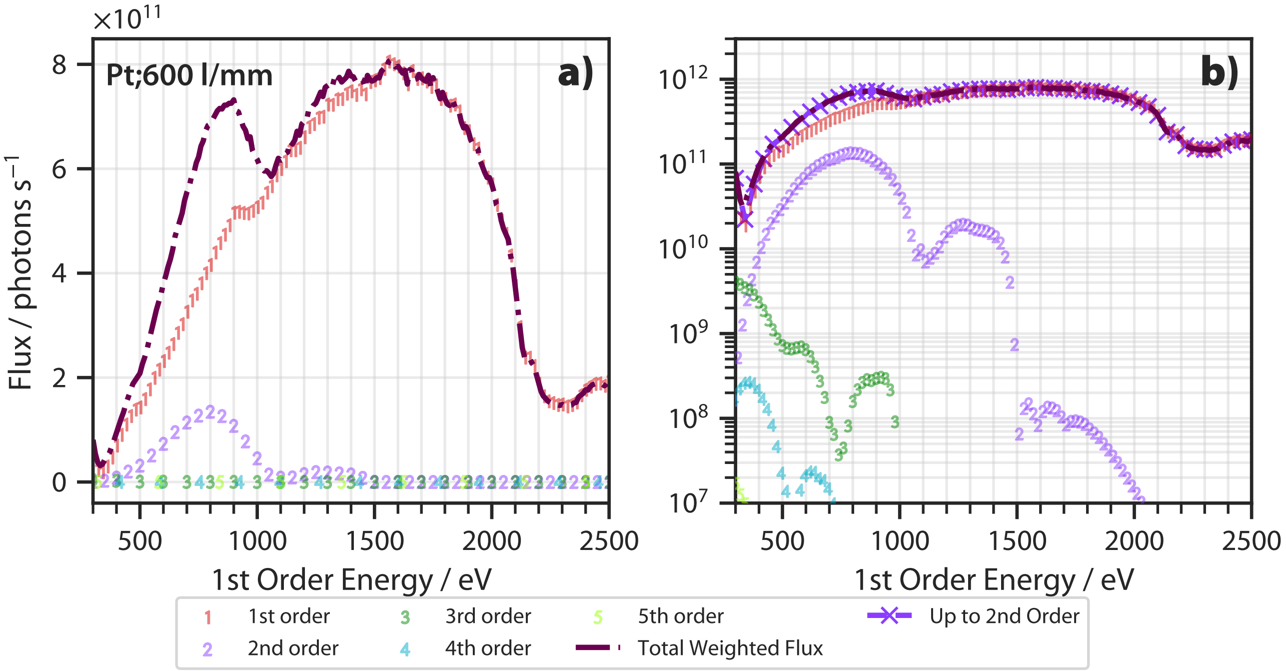

Figure 23: **a)** Simulation results for 600 l/mm grating PGM at c_{ff}=2.0. **b)** the same data plotted on a log y-axis as well as summed flux of first and second order.

3.3 Comparison to Measurements

In a beamline commissioning paper published by Held *et al.* [5], the total flux transmitted by the 400 l/mm grating PGM as well as the 600 l/mm grating PGM is measured with a photodiode. This allows for the direct comparison to simulation results. Due to the physics of the photodiode, which is more sensitive to the higher orders at higher energies, the measured flux is equivalent to the aforementioned weighted total flux. For both 400 and 600 l/mm, the simulated total flux (solid red lines), simulated first order flux (dashed purple lines), and the measurements as reported in literature (green lines marked by dots) are presented in Fig. 24a and c. Fig. 24b and d plots the ratio of the simulated total flux to measurement for the 400 l/mm and 600 l/mm configurations respectively.

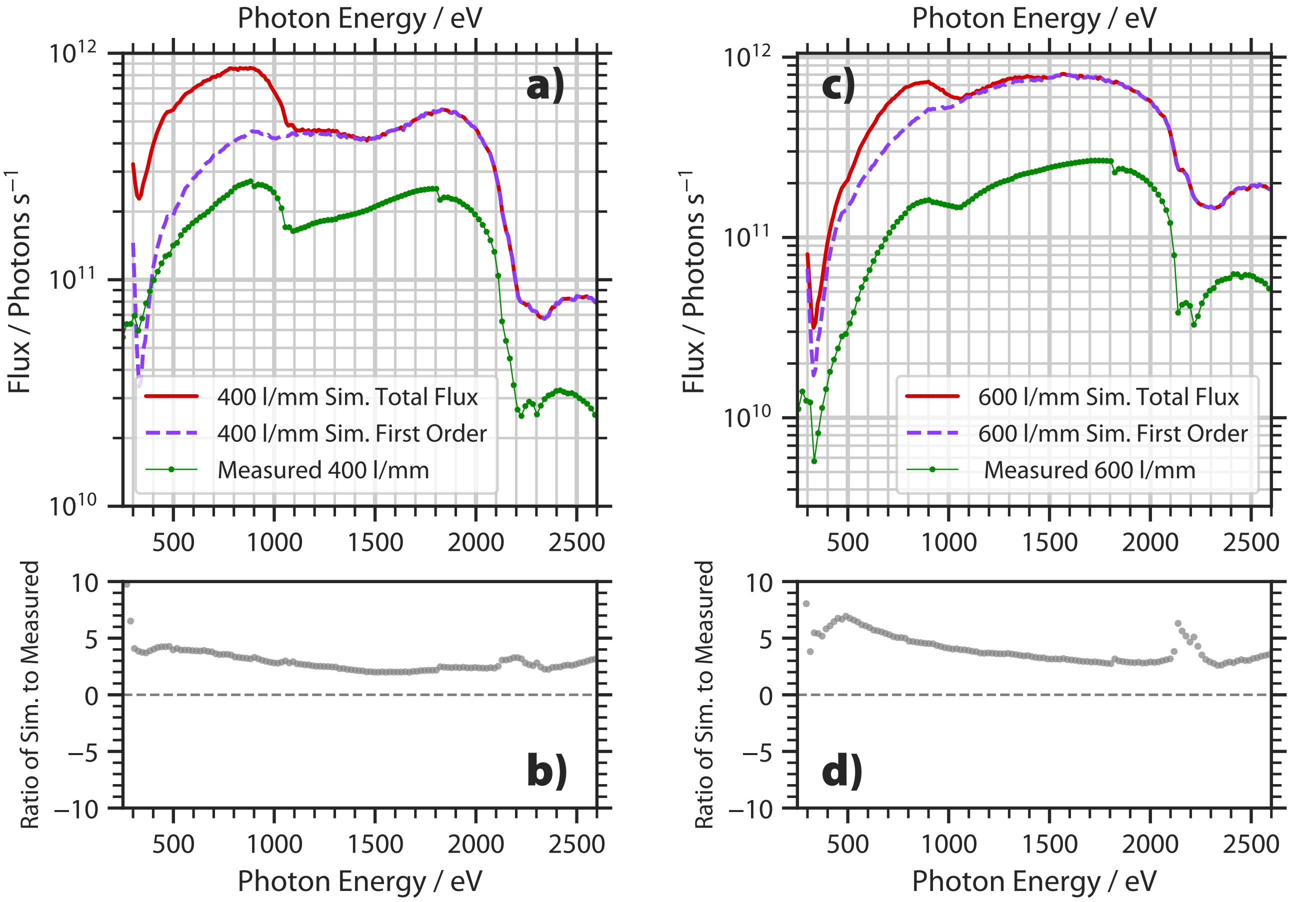

Figure 24: **a)** Simulated results (red) and the first order component (dashed purple) compared to the measured Pt mirror with 400 l/mm grating combination at a c_{ff} value of 2. **b)** The ratio of simulation to the measured flux in a). **c)** and **d)** are the equivalent plots to a) and c) for the 600 l/mm grating. Experimental data courtesy of Prof G. Held [5].

In both Fig. 24a and c, qualitatively, the simulated total flux highly resembles that of the measurements. The simulated flux falloffs are concordant to measurements both in the energy where the falloffs reside, as well as the relative magnitude of the drop. The observed decrease in flux in both simulation (red) and measurement (green) in Fig. 24a at ca. 1000 eV is most likely due to the fall off of reflectivity of the Pt mirror for the second order. This can be clearly seen in Fig. 21a). This directly confirms the presence of higher orders, at the very least second. The second falloff at ca. 2100 eV is the expected Pt M-edge in the first order. In comparison with the first order only flux in Fig. 24a) (purple dashed), the measured flux has discernable features that negate the possibility of a pure first order transmittance.

The flux in units of photons per second, however, is different between calculation and measurement. While the measured flux peaks at 2×10^{11} photons s^{-1} (900 eV), the simulation peaks at 8×10^{11} (900 eV) because the efficiency of the overall beamline is subject to a large number of variables, many of which are simplified or neglected in simulation, *i.e.*, misalignment of optics, or the presence of oxidation on the optic surface. Though the Pt and Au are not particularly susceptible to oxidation by elemental oxygen, the formation of the much more reactive ozone induced by the radiation is capable of reacting with the surface coating. Specifically at B07c, the optics are kept in the presence of oxygen, to take advantage of reactivity of the ozone to remove carbon contamination from the optic surface. The mechanism of carbon contamination is not well known, but the consensus is that the steel vacuum chamber walls are a source of carbon atoms [39]. The precise effect of oxidation on a optic surface apropos of its reflectivity is not well studied, but one can expect added structure near absorption edges, as observed in Fig. 24. Reassuringly, the *pseudo-residual* plots Fig. 24b and d show that disagreements between measurement and simulation mainly manifest in the form of a multiplicative systematic offset of 3-5. Where this deviates, additional structures are observed in the measurement data that are not otherwise seen in simulation, *i.e.* troughs near the Pt absorption edge at 2100 eV which is likely due to the aforementioned oxidation, as well as the ‘notches’ at ca. 900 and 1800 eV. The notches can be attributed to the K-edge absorption, at first and second order energies, by silicon in the photodiode used to measure the flux. A likely explanation of the difference of total flux could be attributed to the fact that not all the slits in the beamline were open at the time of measurement. Though the optical scheme diagram presented one slit, there are many more which were not shown.

3.4 Suggested Mode of Operation

Experimentally, such higher-order contamination can be detrimental to the quality of data. Suppose the sample being tested contains two elements with the absorption edge of one roughly double that of the other, *i.e.*, cobalt's L-III edge at 793.2 eV and nitrogen's K-edge at 409.9 eV [14]. The presence of radiation at both energies would mean that it would be impossible to distinguish between the two species' signals. Indeed, the beamline now almost operates exclusively at a c_{ff} of 1.4, at a significant cost to the flux in the upper end of the energy range (Fig. 20). Using the detailed ray-tracing results, an optimised mode of operation can be derived, which was one of the goals of this work.

There are two factors of consideration, one of first order flux and the other of higher order transmission. As the first order flux is the one correct in energy specified by the user, it stands to reason that it should be maximised. The first order flux for the 400 l/mm grating PGM as a function of c_{ff} and energy is plotted in Fig. 25 a). In Fig. 25 b), the same information is shown, but each point was normalised to the maximum flux at the same energy. This allows the visualisation of flux information in the region where the flux is generally low, past the Pt edge. Brighter areas (closer to value of 1.0) represent energy-c_{ff} combinations where first order flux dominates, darker regions - the opposite. Generally, from Fig. 25 b), the optimal c_{ff} for an energy is oscillating about the mean of ca. 2.0. One may be tempted without knowledge of the extent of higher order transmission to operate at that c_{ff}. However, it was previously observed that c_{ff}=2.0 suffered significant higher order contamination. The second factor of higher order suppression needs to be considered in conjunction with that of the first order flux. Conventional flux measurements that are done in practice are not energy resolved and thus can be deceiving.

The goal is simple: maximise first order flux and maximise higher order suppression. Mathematically, this is can be done by the introduction of a figure of merit (FoM) function. Akin to χ^2 in regression, a FoM is a metric to indicate how well the prescribed conditions are satisfied given a set of data. In a similar work done by Sokolov and colleagues at BESSY II (a synchrotron source in Berlin) where a design of a higher order suppressor is proposed for their metrology beamline in the extreme UV region [36, 40]. Sokolov *et al.* proposed a FoM function of the form:

$$\mathrm{FoM}_{\mathrm{Sokolov}} = \log_{10}(S_2) \times F_1 \tag{28}$$

$$S_2 = \frac{F_1}{F_2} \tag{29}$$

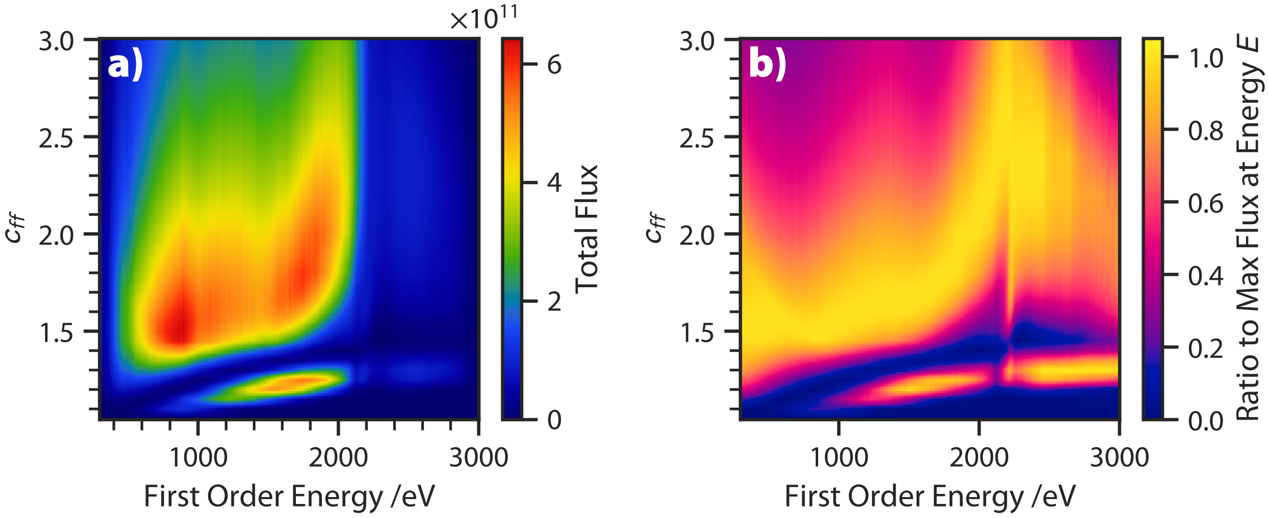

Figure 25: First order flux of the 400 l/mm grating PGM as a function of c_{ff} and energy **a)**; and the same plot where the flux is normalised to the maximum flux for each given energy, **b)**. 2D linear interpolation was used.

where S_2 is the suppression of second order, F_1 and F_2 are first and second order fluxes respectively. This is a purely empirical equation that balances the preference between first order flux and higher order suppression in the use case appropriate to Sokolov *et al.* The choice was made by them to omit orders higher than two, as the grating efficiency decays significantly leading to low transmission and reflectivity, which is in agreement with what we have observed in this work. The $\text{FoM}_{\text{Sokolov}}$ was calculated using the simulation results corresponding to the 400 l/mm grating PGM, Fig. 26. In a), the FoM is plotted as written in Eq. (28), and in b), the per-energy-normalised equivalent of a). The effect of the FoM function can be clearly observed, as the preference for first order flux alone has diminished. Up to 1000 eV, where first order flux is high, the transmission of second order is also high. The sudden increase in the FoM function at ca. 1100 eV causing a discontinuity can again be attributed to second order M-edge absorption by Pt. In Fig. 26b, a rough least-squares fit is provided with the primary intention of providing a quick, on-the-fly functional form that can be used to give an estimate of the best c_{ff}-energy combination. A simple square root function was used:

$$f(x) = a\sqrt{b(x-c)} + d \tag{30}$$

with best-fitting parameters: $a = 0.582$, $b = 2.77\times10^{-3}$, $c = 283$, and $d = 0.797$ for the 400 l/mm grating PGM. Though the general qualitative feature suggests that the FoM as proposed by Sokolov *et al.* may be helpful, it lacks tunability. The function is a purely empirical one, found through trial and

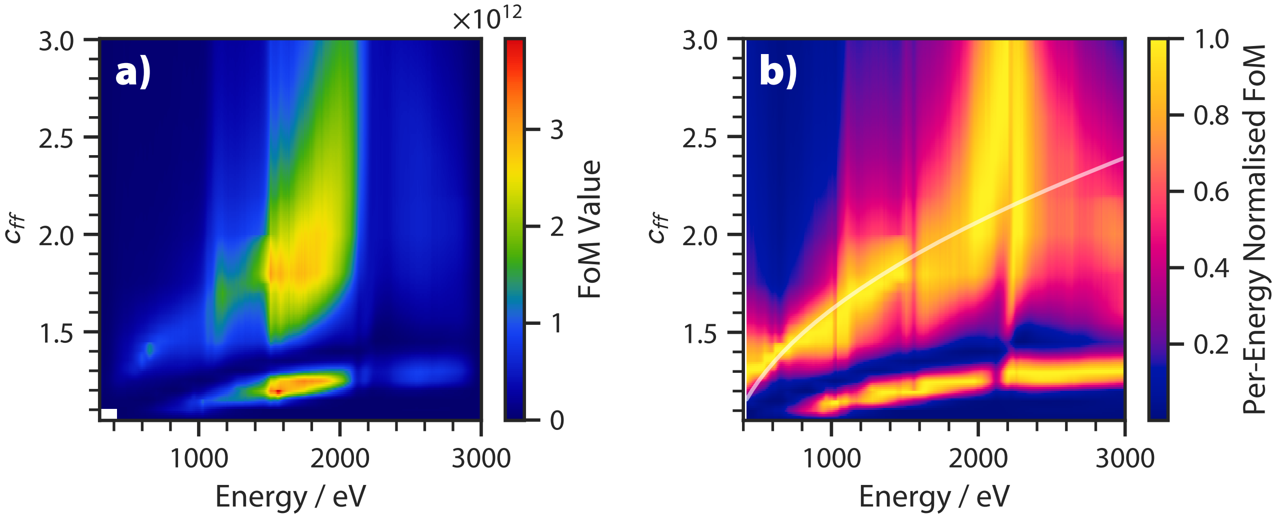

Figure 26: **a)**: The $\text{FoM}_{\text{Sokolov}}$ function as applied to the B07c 400 l/mm grating PGM, and **b)**: data from a) normalised per energy, in the same way as Fig. 25. Note the discontinuity at 1100 eV due to the second order Pt M-edge absorption; the same absorption happens at ca. 2000 eV for the first order. The semi transparent line shows a simple, rough fit through the maxima to offer an accessible 'rule-of-thumb'.

error and is optimised to cater the needs of the metrology beamline at BESSY-II operating in the extreme UV range. In experiments where absorption signals are expected to be weak, the extra flux may outweigh the consideration for spectral purity. Building upon Eq. (28), the following FoM function is proposed:

$$\text{FoM} = \log_{10}(S_2)^{\varepsilon} \times F_1 \tag{31}$$

where ε takes value between 0 and ∞ and all other terms remain the same. The ε term parametrises the balance between the two parameters. In the extreme cases, where ε approaches 0, the first term becomes unity, weighing the FoM entirely on first order flux. For ε larger than one, the effect of higher order suppression is enhanced. This can be seen in Fig. 27. The appropriate value for ε is left to the user to decide, as it will be outside the scope of this work. For example, if $\varepsilon = 1.7$, where the higher flux is favoured, one can apply a logical mask to the per-energy normalised FoM. The brFig. 28 demonstrates the same normalisation process as before in a) and applying a filter where the normalised function value must be greater than 0.99. This allows the direct and quick determination of optimal c_{ff} settings for any given energy. The most optimal combinations are represented as brighter areas in Fig. 28a, and the black areas in b are where the condition that the FoM is greater than 99% of the per energy normalised value. This offers an straightforward alternative to functional fitting presented previously. The optimal c_{ff}-energy pairs are then those coordinates located within the bounds of the dark region. In the case of $\varepsilon = 1$, the FoM$_{\text{Sokolov}}$ is recovered.

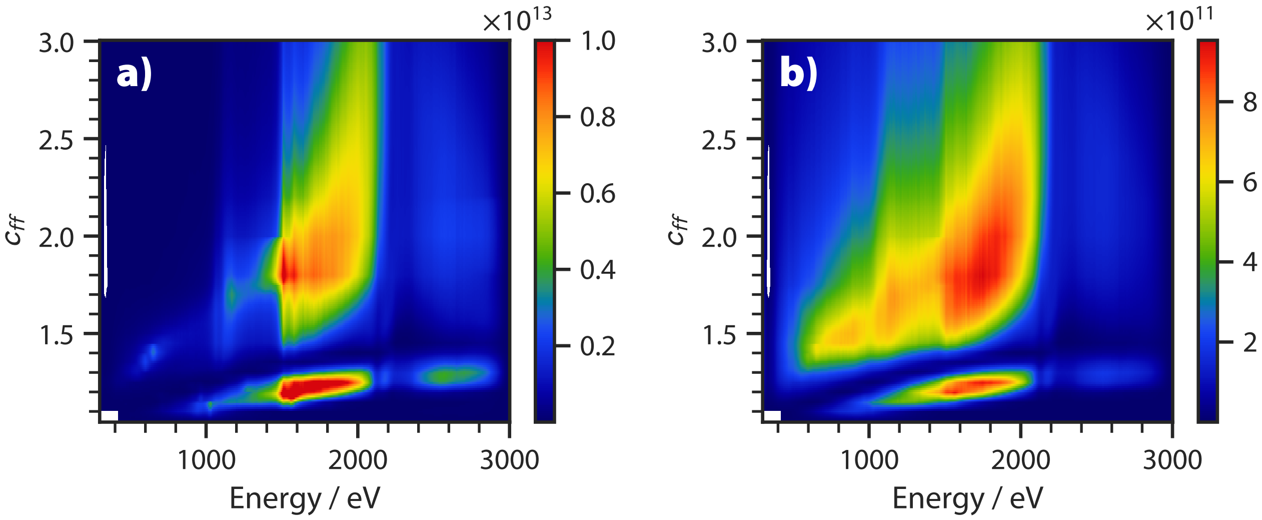

Figure 27: The adapted FoM with **a)** $\varepsilon = 0.6$ and **b)** $\varepsilon = 1.7$

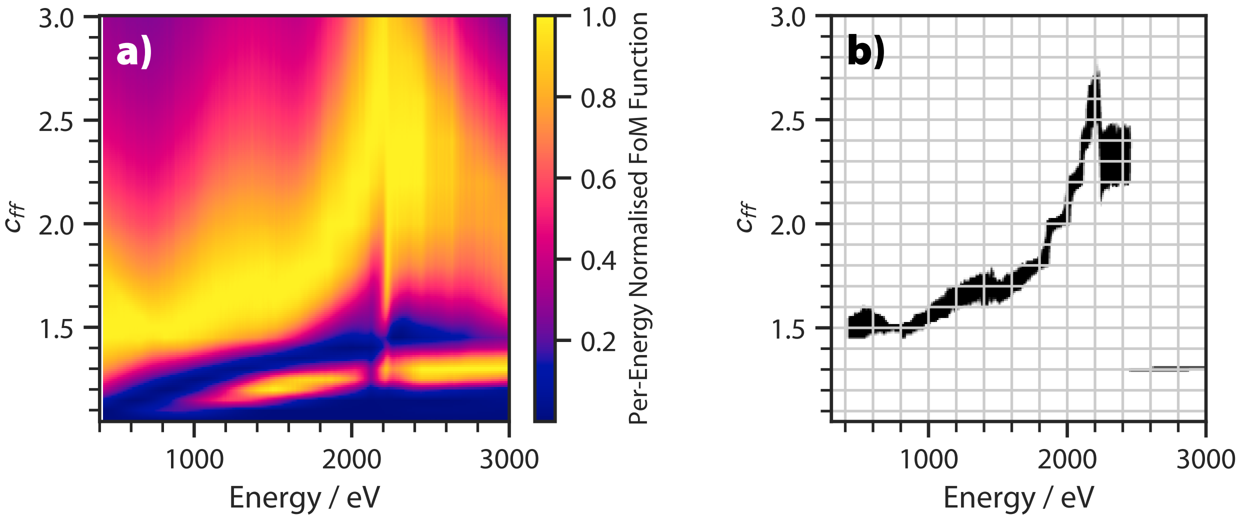

Figure 28: The proposed methodology applied to the FoM with $\varepsilon = 1.7$: **a)**: the per-energy normalised FoM function, and **b)**: the same data as a) but where pixels of less than 0.9 are set to white.

4 Conclusion and Future Outlooks

This thesis set out to develop a set of new methodologies which allow for accurate ray-tracing simulations of soft x-ray beamlines to be carried out. Specifically the plane grating monochromator (PGM) geometry is examined in detail with analytical expressions of important geometrical quantities within the PGM derived. A collection of tools, including a python library to compute PGM geometries and a pre-processor library that is capable of interacting with *SHADOW*, the ray-tracing programme, as well as a novel ray-tracing energy optimisation algorithm, are presented and compiled. These tools serve to establish a better workflow for future simulations of soft X-ray beamlines.

This set of newly proposed methodologies and code were used to carry out a systematic simulation of the B07c beamline at Diamond, where staff have reported anecdotal evidence of higher order contamination. The simulation results were highly convincing in replicating larger structures of the energy spectrum of the beamline. Viewing the data holistically, a set of recommendations were be made. The 600 l/mm grating offers both superior first order flux and higher order suppression. Though not explicitly explored in this work, the higher line density gratings will also offer a higher energy resolution. Consequently, the 600 l/mm grating should be used in most instances in the energy range of 500-3000 eV. The 400 l/mm grating's performance is superior in energies lower than 500 eV. In the fringe energy range nearing the lower limits of the beamline, 400 l/mm grating can be used to extend that range, though the performance in terms of both flux and spectral purity is in no way ideal. To aid decision making, an adapted figure of merit (FoM) function is proposed based on the work of Sokolov *et al.* [40]. A simple fitting of the maxima of the FoM function demonstrates that useful information practical to the beamline users can be easily derived.

As part of the proposed 'toolkit', the transfer function plot was used as a diagnosis visualisation aid. This method allows for the direct visualisation of the ray-traced intensity after each optical element (OE), highlighting the effects said OE. During the validation of ray-tracing results, a deficiency of the library `xraylib` was discovered. Likely due to the fact that previous ray-tracing simulations seldom involved energy step sizes as fine as those used in this work (10 eV), the linear interpolation of the optical constants manifested as unphysical artefacts on the transfer function plot. This demonstrates the need for the development of a standard, reliable optical constants library which should be used in soft X-ray simulations, with data published by Henke *et al.* a good candidate [33].

The practical ray-tracing of this work primarily surrounded that of minimising the effect of higher harmonic contamination. Though the methodology established can be applied to simulate any beamline property of interest, *i.e.*, resolution. In the ray-tracing calculations carried out, the exit slits of the PGM are fixed to be 100 microns. In reality, this size would be adjusted in operation. A holistic simulation encompassing all beamline performance markers can be carried out with the readily available tools that this work has established. At an even higher level, the work done here allows for extensive simulation which can potentially optimise PGM gratings during design. The established workflow reduced the amount of human input needed to a minimum, making iterative simulations across energies, c_{ff} values, line densities *etc.* time efficient and straightforward.

A subset of work conducted here, including the programmatic implementation of the PGM simulation, the optimisation algorithm, and the detailed description of the PGM geometry are expected to be published in an international journal to inform the wider synchrotron radiation community of the progress.

References

[1] J. E. N. Swallow, E. S. Jones, A. R. Head, J. S. Gibson, R. B. David, M. W. Fraser, M. A. van Spronsen, S. Xu, G. Held, B. Eren, and R. S. Weatherup, “Revealing the role of co during co2 hydrogenation on cu surfaces with in situ soft x-ray spectroscopy”, JACS **145**, 6730–6740 (2023).

[2] M. Sanchez del Rio, N. Canestrari, F. Jiang, and F. Cerrina, “Shadow3: a new version of the synchrotron x-ray optics modelling package”, en, J. Synchrotron Radiat. **18**, 708–716 (2011).

[3] P. Willmott, *An introduction to synchrotron radiation, Techniques and applications*, Second edition, Includes bibliographical references and index (John Wiley & Sons, Inc., Hoboken, NJ, 2019), 1483 pp.

[4] S. Mobilio, ed., *Synchrotron radiation, School on synchrotron radiation*, SpringerLink, Description based upon print version of record (Springer, Berlin, Heidelberg, 2015), 799389150 pp.

[5] G. Held, F. Venturini, D. C. Grinter, P. Ferrer, R. Arrigo, L. Deacon, W. Quevedo Garzon, K. Roy, A. Large, C. Stephens, A. Watts, P. Larkin, M. Hand, H. Wang, L. Pratt, J. J. Mudd, T. Richardson, S. Patel, M. Hillman, and S. Scott, “Ambient-pressure endstation of the versatile soft x-ray (versox) beamline at diamond light source”, J. Synchrotron Radiat. **27**, 1153–1166 (2020).

[6] S. B. Wilkins, P. D. Hatton, M. D. Roper, D. Prabhakaran, and A. T. Boothroyd, “Soft x-ray resonant magnetic diffraction”, Phys. Rev. Lett. **90**, 187201 (2003).

[7] J. Fink, E. Schierle, E. Weschke, and J. Geck, “Resonant elastic soft x-ray scattering”, en, Rep. Progr. Phys. **76**, 056502 (2013).

[8] B. A. Collins and E. Gann, “Resonant soft x-ray scattering in polymer science”, J. Polym. Sci. **60**, 1199–1243 (2021).

[9] J. Yano and V. K. Yachandra, “X-ray absorption spectroscopy”, Photosynth. Res. **102**, 241–254 (2009).

[10] U. Bergmann and P. Glatzel, “X-ray emission spectroscopy”, Photosynth. Res. **102**, 255–266 (2009).

[11] J. E. Penner-Hahn, “X-ray absorption spectroscopy in coordination chemistry”, Coord. Chem. Rev. **190–192**, 1101–1123 (1999).

[12] T.-L. Lee and D. A. Duncan, “A two-color beamline for electron spectroscopies at diamond light source”, Synchrotron Rad. News **31**, 16–22 (2018).

[13]H. Petersen, C. Jung, C. Hellwig, W. B. Peatman, and W. Gudat, “Review of plane grating focusing for soft x-ray monochromators”, Rev. Sci. Instrum. **66**, 1–14 (1995).

[14]W. M. Haynes and D. R. Lide, eds., *Crc handbook of chemistry and physics, A ready-reference book of chemical and physical data*, 96. ed., 2015-2016, Includes bibliographical references and index (CRC Press, Boca Raton, Fla. [u.a.], 2015).

[15]T. Tanaka and H. Kitamura, “Spectra: a synchrotron radiation calculation code”, J. Synchrotron Radiat. **8**, 1221–1228 (2001).

[16]K. C. Johnson, *Grating diffraction calculator (gd-calc ®)*, en, 2022.

[17]A. C. Walters, Private Communications (2023).

[18]N. Metropolis and S. Ulam, “The monte carlo method”, J. Am. Stat. Assoc. **44**, 335–341 (1949).

[19]F. Cerrina, *Shadow: user guide* (July 22, 1998).

[20]E. Bergbäck Knudsen, A. Prodi, J. Baltser, M. Thomsen, P. K. Willendrup, M. Sanchez Del Rio, C. Ferrero, E. Farhi, M. K. Haldrup, A. Vickery, R. Feidenhans’l, K. Mortensen, M. M. Nielsen, H. F. Poulsen, S. Schmidt, and K. Lefmann, “Mcxtrace: a monte carlo software package for simulating x-ray optics, beamlines and experiments”, J. Appl. Crystallogr. **46**, 679–696 (2013).

[21]K. Chapman, B. Lai, F. Cerrina, and J. Viccaro, “Modelling of undulator sources”, Nucl. Instrum. Methods Phys. Res., Sect. A **283**, 88–99 (1989).

[22]A. Brunetti, M. Sanchez del Rio, B. Golosio, A. Simionovici, and A. Somogyi, “A library for x-ray–matter interaction cross sections for x-ray fluorescence applications”, Spectrochim. Acta, Part B, 17th International Congress on X-Ray Optics and Microanalysis **59**, 1725–1731 (2004).

[23]S. G. Alcock, K. J. S. Sawhney, S. Scott, U. Pedersen, R. Walton, F. Siewert, T. Zeschke, F. Senf, T. Noll, and H. Lammert, “The diamond-nom: a non-contact profiler capable of characterizing optical figure error with sub-nanometre repeatability”, Nucl. Instrum. Methods Phys. Res., Sect. A **616**, 224–228 (2010).

[24]S. G. Alcock, I. Nistea, and K. Sawhney, “Nano-metrology: the art of measuring x-ray mirrors with slope errors <100 nrad”, Rev. Sci. Instrum. **87**, `10.1063/1.4949272` (2016).

[25]F. Schäfers, “The bessy raytrace program ray”, in *Modern developments in x-ray and neutron optics* (Springer Berlin Heidelberg), pp. 9–41.

[26]A. C. Walters, Publication forthcoming (2024).

[27] M. Neviere and E. K. Popov, “Electromagnetic theory of gratings: review and potential applications”, in Theory and practice of surface-relief diffraction gratings: synchrotron and other applications, Vol. 3450 (Sept. 1998), pp. 2–10.

[28] T.-L. Lee, “Geometrical considerations of a plane grating monochromator”, Unpublished work (2009).

[29] W. B. Peatman, *Gratings, mirrors and slits, Beamline design for soft x-ray synchrotron radiation sources*, Description based on publisher supplied metadata and other sources. (CRC Press LLC, Boca Raton, 1997), 1227 pp.

[30] W. Elam, B. Ravel, and J. Sieber, “A new atomic database for x-ray spectroscopic calculations”, Radiat. Phys. Chem. **63**, 121–128 (2002).

[31] M. J. Berger and J. H. Hubbell, *Xcom-photon cross sections database, nist standard reference database 8*, en, 1987.

[32] E. F. Plechaty, D. E. Cullen, and R. J. Howerton, *Tables and graphs of photon-interaction cross sections from 0. 1 kev to 100 mev derived from the lll evaluated-nuclear-data library* (Nov. 1981).

[33] B. L. Henke, E. M. Gullikson, and J. C. Davis, “X-ray interactions: photoabsorption, scattering, transmission, and reflection at e = 50-30,000 ev, z = 1-92”, At. Data. Nucl. Data Tables **54**, 181–342 (1993).

[34] D. C. Grinter, F. Venturini, P. Ferrer, M. A. van Spronsen, R. Arrigo, W. Quevedo Garzon, K. Roy, A. I. Large, S. Kumar, and G. Held, “The versatile soft x-ray (versox) beamline at diamond light source”, Synchrotron Rad. News **35**, 39–47 (2022).

[35] A. C. Thompson, J. Kirz, D. T. Attwood, E. M. Gullikson, M. R. Howells, J. B. Kortright, Y. Liu, and A. L. Robinson, *Center for x-ray optics advanced light source: x-ray data booklet*, 3rd ed. (Lawrence Berkeley National Laboratory, 2009).

[36] A. Sokolov, M. G. Sertsu, A. Gaupp, M. Lüttecke, and F. Schäfers, “Efficient high-order suppression system for a metrology beamline”, J. Synchrotron Radiat. **25**, 100–107 (2018).

[37] U. Frommherz, J. Raabe, B. Watts, R. Stefani, U. Ellenberger, R. Garrett, I. Gentle, K. Nugent, and S. Wilkins, “Higher order suppressor (hos) for the pollux microspectroscope beamline at the swiss light source sls”, AIP Conf. Proc. **1234**, 429–432 (2010).

[38] *Optical gratings: compendium of principles, manufacture, products and applications* (Carl Zeiss Spectroscopy GmbH, 2013).

[39] R. A. Rosenberg and D. C. Mancini, "Deposition of carbon on gold using synchrotron radiation", Nucl. Instrum. Methods Phys. Res., Sect. A **291**, 101–106 (1990).

[40] A. Sokolov, P. Bischoff, F. Eggenstein, A. Erko, A. Gaupp, S. Künstner, M. Mast, J.-S. Schmidt, F. Senf, F. Siewert, T. Zeschke, and F. Schäfers, "At-wavelength metrology facility for soft x-ray reflection optics", Rev. Sci. Instrum. **87**, `10.1063/1.4950731` (2016).